Title

Early spatial and contextual coding deficits in hippocampal CA1 precede performance decline in an Alzheimer's disease model

Authors

Yimei Li,[1] Mary Ann Go,[1] Hualong Zhang,[1,2] Simon R Schultz[1*]

Affiliations

1. Centre for Neurotechnology and Department of Bioengineering, Imperial College London, United Kingdom
2. Department of Biomedical Engineering, University of Melbourne

Correspondence to: s.schultz@imperial.ac.uk

Abstract

Alzheimer's disease (AD) is characterised by progressive memory decline, yet how hippocampal representations change at early disease stages remains largely unknown. Using a real-world head-fixed spatial alternation task combined with in vivo two-photon imaging, we examined hippocampal CA1 representations in 5xFAD mice. Although 7-12 month old 5xFAD mice exhibited significant impairments in task learning, 2-4 month old mice performed normally, allowing us to assess hippocampal coding before behavioural decline. At this early stage, CA1 neurons showed intact global spatial encoding but impaired task-related place cell representations. Contextual representations revealed by trajectory-dependent coding were weakened at both the population and single cell levels, accompanied by a shift from predominantly retrospective towards more prospective encoding along the central arm. Despite these vulnerabilities, a subset of place cells largely retained stable spatial representations that persisted throughout task learning in early-stage AD mice. Chemogenetic activation of basal forebrain cholinergic neurons improved spatial information rates and stability of spatial and contextual coding in early-stage 5xFAD mice. Together, these findings show that hippocampal spatial and contextual coding is disrupted early in AD, while a subset of stable place cells remains preserved, and that these representational deficits emerge before impairments in spatial alternation behaviour.

Introduction

Alzheimer's disease (AD) is the most prevalent cause of dementia in older adults, particularly affecting individuals over 65 years of age [1]. A central feature of AD pathology is the amyloidogenic processing of amyloid precursor protein (APP), which produces amyloid-β (Aβ) and triggers downstream pathophysiological cascades leading to synaptic dysfunction and neuronal loss [2, 3, 4, 5, 6]. Among the cognitive impairments associated with this pathway, spatial navigation deficits are especially prominent and often emerging as early as the mild cognitive impairment stage [7, 8]. More than 60% of AD patients experience spatial disorientation and wandering behaviour [9]. These deficits are closely linked to hippocampal dysfunction. Hippocampal CA1 neurons, crucial for forming spatial and episodic memories, exhibit abnormalities in morphology, synaptic plasticity, and neurogenesis in AD, in both human patients and mouse models [10, 11, 12].

Hippocampal place cells are essential for supporting spatial navigation and memory formation, and accumulating evidence indicates that their function is disrupted in AD. Impairments in place cell firing have been reported across several AD mouse models, including APP transgenic and APP knock-in lines. For example, 11-16 month age Tg2576 and APP mice show degraded place fields and reduced spatial information, typically in conjunction with behavioural deficits [13, 14]. In 3xTg AD mice, reduced spatial information has been reported in young 3xTg mice during open-field or linear track running , with reduced theta- and slow-gamma phase locking [15, 16]. In 5xFAD mice, impaired synaptic efficacy and weakened sharp wave-ripples have been observed during virtual reality

spatial tasks at 11–14 months of age[17]. Object-discrimination experiments in 4 month-old 5xFAD mice revealed preserved task performance and population coding within the discrimination task, despite reduced spatial coding in other environments [18]. Overall, these findings demonstrate place cell dysfunction in AD, though most evidence comes from later disease stages or from simplified exploratory paradigms rather than behaviourally demanding tasks.

In contrast to place cells, which encode spatial location, splitter cells encode trajectory-dependent contextual information, firing differently on a common path depending on past choices or future decisions. First identified in continuous alternation tasks in rats [19, 20], splitter cells integrate retrospective and prospective information within single CA1 neurons and are thought to support flexible navigation [21]. Despite their importance, little is known about how splitter cell activity is affected in AD. Given that Aβ-related synaptic changes impair hippocampal learning [22] and that splitter cell activity depends on rapid synaptic plasticity [23], trajectory-dependent contextual coding may be particularly vulnerable early in the disease.

Here, we developed a real-world head-fixed continuous T-maze alternation task that imposes goal-directed spatial learning demands comparable to those in freely moving paradigms[24, 25]. We combined this task with two-photon calcium imaging in 5xFAD mice, which begin to accumulate amyloid pathology around 2-4 months of age due to APP and presenilin-1 mutations[26, 27], allowing us to record CA1 neuronal activity during task

performance. This approach enabled us to examine how spatial coding and trajectory-dependent contextual representations in CA1 are altered during the early stage of AD. Given the established role of basal forebrain cholinergic input in modulating hippocampal synaptic plasticity[28], we further tested whether enhancing cholinergic activity could improve CA1 encoding in early-stage 5xFAD mice.

Results

1. A head-fixed alternation task reveals preserved spatial learning in 2- 4 month old 5xFAD mice and emerging deficits with age

We developed a novel behavioural paradigm to assess spatial memory in head-fixed mice, in which animals performed a continuous spatial alternation task within a real-world, air-lifted Y-maze (Fig. 1a, left). Mice received a 4 µl of liquid reward only when they entered the arm opposite to the one visited in the previous trial (Fig. 1a, right). Water-restricted mice expressing GCaMP7s in CA1 pyramidal neurons of the dorsal hippocampus were trained to perform the task while calcium activity was simultaneously recorded using two-photon microscope (Fig. 1b).

Consistent with previous reports, amyloid plaques were observed in 5xFAD mice at 2-4 months ages and became extensive in the hippocampal CA1 region at 7-12 months [29, 30]. (Supplementary Fig. 1a). We therefore focused on these two age groups to examine task performance. In 2-4 month-old 5xFAD mice, the percentage of correct trials was

comparable to age-matched controls (Genotype × Day, β = -1.29, 95%CI [-2.63, 0.44], p = 0.16, linear-mixed effect mode (LMM); Fig. 1c,d). In contrast, 7-12 month-old 5xFAD mice were exhibited pronounced learning impairments (Genotype × Day, β = -2.56, 95%CI [-4.57, -0.54], p = 0.013, Fig. 1f,g). Notably, aged 5xFAD mice also showed greater variability in the number of trials completed per day, potentially affecting learning opportunities (Supplementary Fig. 1b,c,f,g). To account for this, trials from all sessions were grouped into consecutive 50-trial blocks, and the percentage of correct trials was calculated per block (Supplementary Fig. 1d, h). The analysis yielded results consistent with day wise performance: 2-4 month-old 5xFAD mice displayed no significant behavioural deficits (Genotype × Block, β = 0.35, 95%CI [-0.70, 1.40], p = 0.51; Fig. 1e), whereas 7-12 month-old mice showed a significant impairment (Genotype × Block, β = -1.85, 95%CI [-3.63, -0.06], p = 0.043; Fig. 1h).

Furthermore, the proportion of 7-12 month-old 5xFAD mice reaching the task acquisition criterion was significantly reduced compared to controls, whereas the 2-4 month-old group showed normal acquisition rates (Supplementary Fig. 1e,i). These findings indicate that spatial learning deficits are evident in 5xFAD mice by 7-12 months of age, consistent with previous studies [27], while 2-4 month-old 5xFAD mice retain intact task performance.

To evaluate the overall spatial coding capacity of CA1 neurons, we quantified global spatial information, defined as the Skaggs' spatial information content computed from two-dimensional spatial activity maps across all trajectories within the imaging session. In 2–4 month-old 5xFAD mice, CA1 neurons exhibited spatial information levels comparable to controls (β = -0.12, 95% CI [-0.89, 0.66], *p* = 0.77; LMM; Fig. 1i, left).

124 Similarly, the proportion of neurons meeting the place cell criterion showed a non-
125 significant reduction (rrb = -0.25, p = 0.25; Fig. 1i, right). In contrast, 7-12 month-old
126 5xFAD mice displayed significant impairments in spatial coding, as reflected by reduced
127 global spatial information (β = -0.54, 95% CI [-1.00, -0.09], p = 0.019; Fig. 1j, left) and a
128 lower proportion of place cells (rrb = -0.67, p = 0.015; Fig. 1j, right). Together, these
129 results demonstrate that while 2-4 month old 5xFAD mice retain intact spatial learning
130 and CA1 global spatial coding during spatial alternation task, both behavioural
131 performance and neuronal spatial representations impaired markedly by 7-12 months of
132 age.

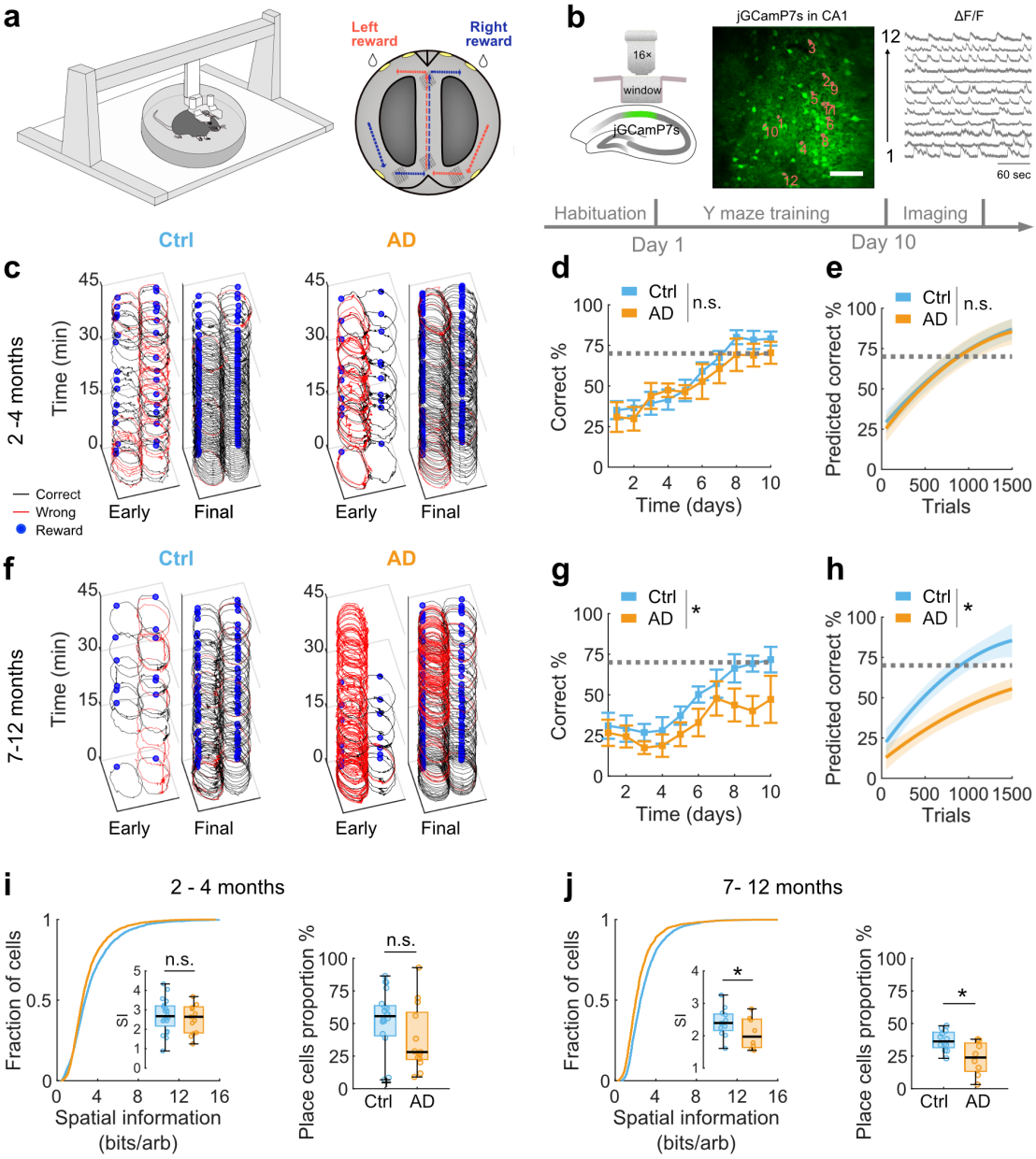

Figure 1. Impairments in behavioural deficits and CA1 spatial representations in 5xFAD mice during the spatial alternation task

a. Left: Schematic illustration of a head-fixed mouse navigating an air-lifted figure-8 maze. Right: Bird's eye view of the same maze, with correct trials highlighted in blue (left-to-right) and red (right-to-left).

b. Schematic of in vivo calcium imaging from CA1 pyramidal neurons expressing jGCaMP7s. Twelve example regions of interest (ROIs) are overlaid on the imaging field of view, with corresponding calcium ΔF/F traces shown right. Scale bar: 100 μm.

c. Representative temporal trajectories of mouse navigation on early and final training days (2–4 months of age). Correct trials are shown in black, and error trials in red. Reward zones are indicated by blue dots.

d. Learning curves showing the percentage of correct alternation trials over training days in 2–4 month-old mice. The horizontal dotted line indicates the 70% performance crietria. Control (Ctrl; n = 10 mice) vs. 5xFAD (AD; n = 7 mice). Genotype × Day interaction, linear-mixed effect mode (LMM).

e. Trials across all sessions were binned into consecutive 50-trial blocks, with the percentage of correct% calculated per block (Genotype × Block interaction). Curves show quadratic mixed-effects model fits, with shaded areas indicating 95% confidence intervals.

f - h. Same as in panels **c - e**, but for mice aged 7–12 months (Ctrl: n = 6 mice; AD: n = 6 mice).

i. Left: Cumulative distribution of Skagg's spatial information for all detected CA1 neurons, based on 2D spatial maps from 2-4 month-old mice. Inset: session level medians. LMM test. Right: Proportion of neurons classified as place cells per session. Two-sided Wilcoxon rank-sum test. Ctrl: n = 4397 cells from 20 imaging sessions (10 mice) ; AD: n = 3073 cells from 13 sessions (7 mice).

j. Same as panel **i**, for mice aged 7-12 months. Ctrl: n = 2168 cells from 12 imaging sessions (6 mice); AD: n = 1477 cells from 8 sessions (6 mice).

2. Disruption of CA1 place cell coding during task-related trajectories in 2-4 month old 5xFAD mice.

Understanding the early stage of AD is crucial for identifying initial circuit level disruptions and informing early intervention [31, 32]. Based on our behavioural and neuronal observations (Fig. 1c-j), together with prior reports indicating that hippocampal long-term potentiation and detectable hippocampal-dependent behavioural deficits emerge after 6 months of age in 5xFAD mice [29, 33, 34], we focused on 2-4 month old 5xFAD mice to examine early alternations in hippocampal neural coding.

To assess task-related spatial representations, we linearised trajectories and generated one-dimensional spatial activity maps during the post-acquisition phase, when mice consistently performed the alternation task. Analyses were restricted to correct trials, which most directly reflect task engagement. This yielded a measure of spatial coding specifically aligned with behavioural performance, in contrast to global spatial metrics. At the population-level, spatial stability was quantified by calculating population vector (PV) correlations between odd and even trials across all CA1 neurons within each imaging session (Fig. 2a). 2-4 month old 5xFAD mice exhibited significantly reduced PV correlations compared to controls (rrb = -0.45, p = 0.031; Fig. 2b), indicating impaired population level spatial consistency despite intact behavioural performance (Supplementary Fig. 2a-e).

We next examined spatial coding stability at the single cell level by analysing CA1 place cell activity during correct trials (Fig. 2c). In 5xFAD mice, place cells showed a trend

185 toward reduced spatial information relative to controls (β = -0.24, 95% CI [-0.48, 0.006],
186 p = 0.056; LMM; Fig. 2d). Trial-to-trial tuning curve correlation, a measure of place cell
187 stability, was significantly lower in 5xFAD mice (β = -0.02, 95% CI [-0.04, -0.002], p =
188 0.029; Fig. 2e,f), indicating decreased consistency of spatial representations across
189 repeated trajectories. To further examine spatial coding stability, we quantified (i) the
190 active trial ratio, defined as the proportion of trials in which a place cell was active within
191 its place field, and (ii) the tuning curve correlation across adjacent active trials. Both
192 measures were significantly reduced in 5xFAD mice (Supplementary Fig. 2f,g), further
193 supporting disrupted trial-wise spatial coding. Place field fidelity was assessed using two
194 measures: (i) in-field versus out-of-field selectivity, which showed a non-significant trend
195 towards reduction (β = -0.04, 95% CI [-0.08, 0.002], p = 0.064; Fig. 2g); and (ii) peak in-
196 field activity, which was significantly lower in 5xFAD mice (β = -0.33, 95% CI [-0.57, -0.08],
197 p = 0.0097; Fig. 2h). Together, these results suggest that CA1 place cells in early-stage
198 5xFAD mice exhibit reduced spatial encoding stability and weakened peak activity within
199 place fields.

200

201 Importantly, behavioural performance and locomotion were preserved during imaging
202 sessions (Supplementary Fig. 2a-e), confirming that neuronal deficits were not driven by
203 overt behavioural changes. Additionally, in both groups, place cell stability and fidelity
204 differed between correct and error trials (Supplementary Fig. 2h-l), indicating the task-
205 dependence of CA1 spatial coding. Together, these findings show that CA1 spatial coding
206 is already impaired in early-stage 5xFAD mice, with reduced population stability, weaker

207 place field activity, and less reliable single cell responses during alternation task-related

208 navigation.

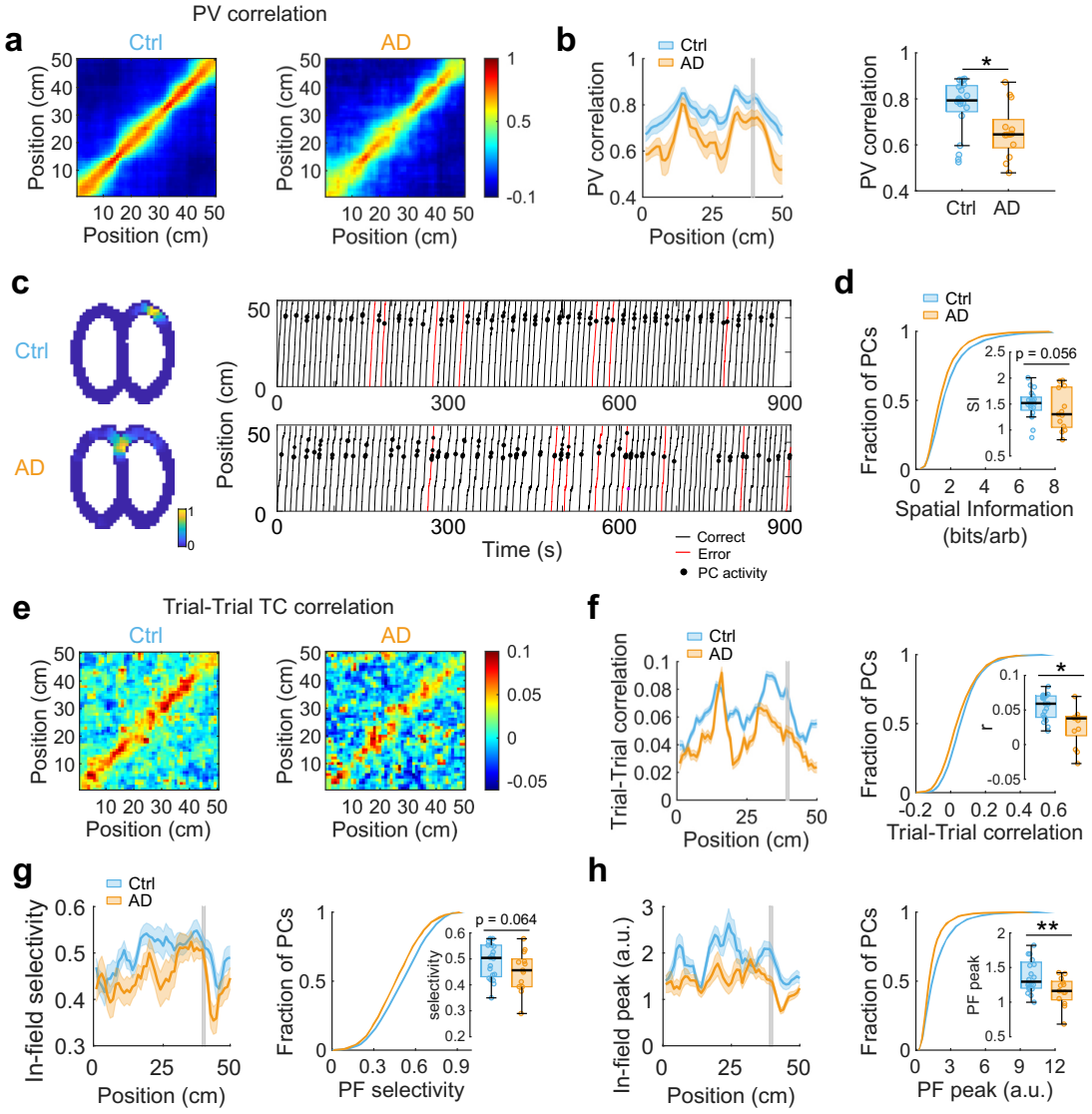

209

210

211 **Figure 2. Impaired CA1 place cells during correct trials in 2-4 month-old 5xFAD mice.**

212

213 **a.** Population vector (PV) correlations between odd and even trials for all detected CA1 neurons,

214 averaged across animals within each group.

b. Left: Diagonal PV correlation coefficients plotted along the linearised trajectory. Right: Mean diagonal PV correlation for each imaging session. Shaded areas represent mean ± s.e.m. across sessions. Grey shading indicates reward locations. Two-sided Wilcoxon rank-sum test.

c. Representative CA1 place cells recorded from control and 5xFAD mice (2–4 months). Left: Normalised two-dimensional spatial rate maps. Right: Linearised positional trajectories showing place-cell activity across trials. Black lines denote correct trials; red lines denote error trials; black dots indicate calcium events from place cells.

d. Cumulative distributions with inset box plots showing the median spatial information of CA1 place cells in control and 5xFAD mice.

e–f. Trial-to-trial tuning-curve correlations of place cells. Pearson correlation coefficients plotted along the linearised trajectory. Shaded areas denote mean ± s.e.m. across cells. Cumulative distributions of mean diagonal tuning-curve correlations across all place cells with inset box plots showing the median value for each imaging session.

g. Same analysis as in f, but for in-field versus out-of-field selectivity, calculated as (in-field − out-of-field) / (in-field + out-of-field).

h. Same analysis as in g, but for the peak in-field activity of place cells.

Statistical comparisons in panels **d–h** were also performed using LMM. Ctrl: n = 4397 recorded cells, n = 2952 place cells from 20 imaging sessions (10 mice); 5xFAD: n = 3073 recorded cells, n = 1791 place cells from 13 imaging sessions (7 mice).

3. A stable subset of CA1 place cells is preserved across learning in early-stage 5xFAD mice

The long-term stability of hippocampal place cells is thought to support the spatial memory retention [35, 36]. To assess whether learning related spatial representation stability

239 is altered in early-stage 5xFAD mice, we tracked the same CA1 neuronal populations
240 across three task acquisition stages: early (day 6), middle (day 8), and final (after day 10)
241 (Fig. 3a). Place cells were identified at each stage and stable place cells were defined as
242 neurons that (i) exhibited a place field at all stages and (ii) showed tuning-curve (TC)
243 correlations between adjacent stages exceeding a predefined threshold (>0.51;
244 Supplementary Fig. 3c; Methods). This approach isolated neurons maintaining consistent
245 spatial representations across learning (Fig. 3b-d; Supplementary Fig. 3d).

246 Behavioural alternation performance did not differ between groups (Genotype × Stage: p
247 = 0.61, LMM; Supplementary Fig. 3a). The proportion of stable place cells relative to all
248 recorded cells was similar between groups (Ctrl: 14.7 ± 2.2%; 5xFAD: 14.1 ± 2.9%; p =
249 1; Fig. 3e). Likewise, the proportion of stable cells among all place cells did not differ at
250 any stage (stage 1: rrb = 0.09, p = 0.89; stage 2: rrb = 0.06, p = 0.89; stage 3: rrb = 0.37,
251 p = 0.23; Fig. 3e). TC correlations of stable place cells between stages were unchanged
252 (stage 1-3: rrb = 0.12, p = 0.56; stage 1-2: rrb= 0.007, p = 0.91; stage 2-3: rrb = 0.07, p =
253 0.25; Fig. 3f). The within session trial-to-trial TC correlations (stage 1: rrb = 0.03, p = 1;
254 stage 2: rrb = -0.2, p = 0.60; stage 3: rrb = 0.13, p = 1; Fig. 3g), in-field selectivity (stage
255 1: rrb = -0.02, p = 1; stage 2: rrb = 0.05, p = 0.70; stage 3: rrb = -0.09, p = 0.68), and peak
256 in-field activity (stage 1: rrb = -0.13, p = 0.46; stage 2: rrb = -0.07, p = 1; stage 3: rrb = -
257 0.12, p = 0.59; Fig. 3g) were not changed in 5xFAD mice. By contrast, unstable place
258 cells (Fig. 3d) showed significantly reduced trial-to-trial TC correlations (stage 1: rrb = -
259 0.06, p = 0.15; stage 2: rrb = -0.18, p < 0.001; stage 3: rrb = -0.13, p < 0.001; Fig. 3h), in-
260 field selectivity (stage 1: rrb = -0.1, p = 0.04; stage 2: rrb = -0.04, p =0.89; stage 3: rrb =
261 -0.07, p =0.23) and peak in-field activity (stage 1: rrb = -0.22, p< 0.001; stage 2: rrb = -

0.17, p< 0.001; stage 3: rrb = -0.09, p =0.03) across the majority of learning stages. Thus, despite spatial coding deficits in unstable place cells, early-stage 5xFAD mice preserve a subset of stable place cells whose coding properties and prevalence remain intact across learning.

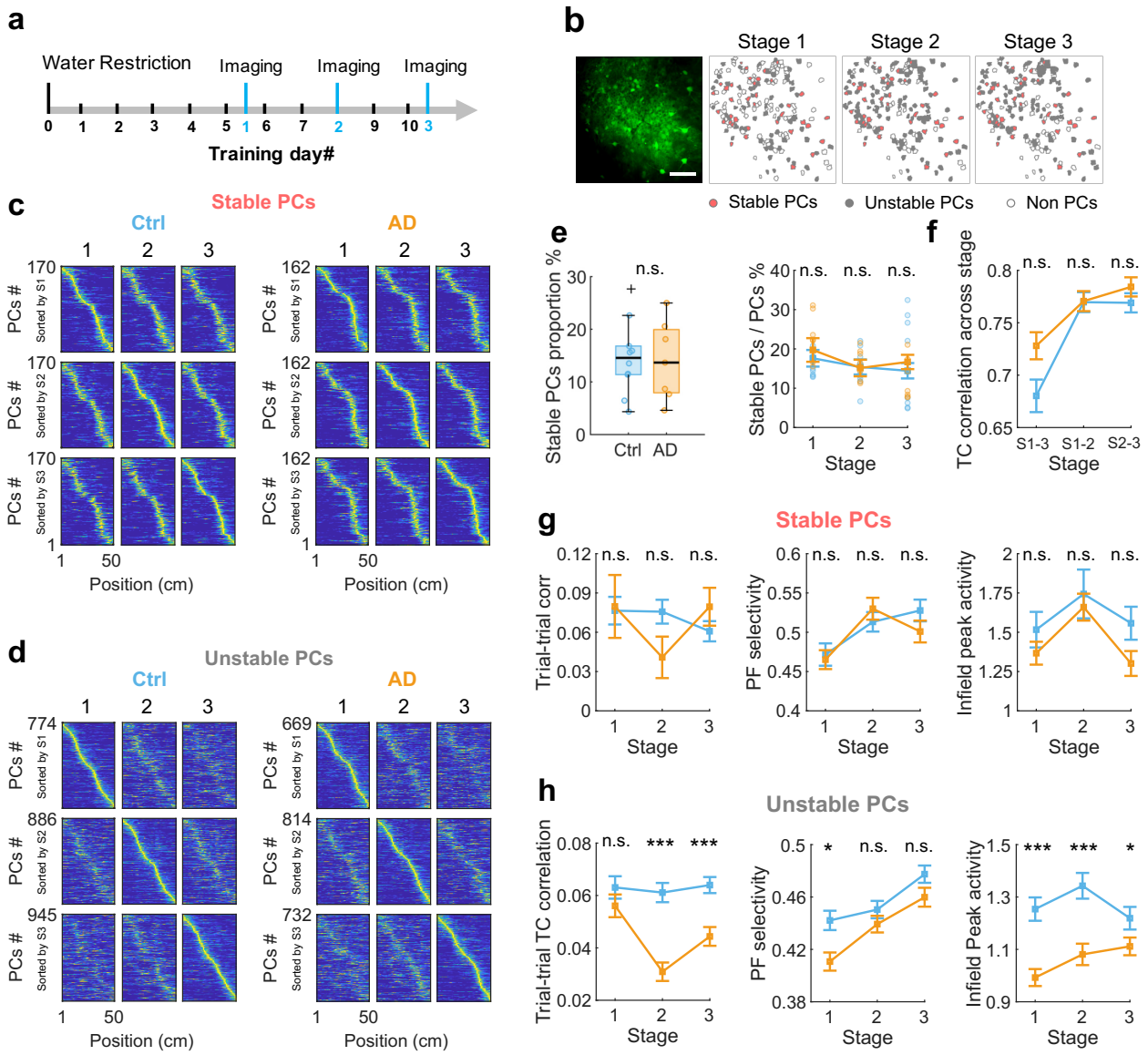

Figure 3. Spatial representations across training stages in early-stage 5xFAD mice

a. Timeline of imaging sessions during task acquisition, including early-stage imaging (around the 6th training day), middle-stage imaging (around the 8th training day), and late-stage imaging (after the 10th training day).

b. Example CA1 FOV showing identified place cells at each stage in a 5xFAD mouse. Red contours indicate stable place cells that maintained stable spatial tuning across all stages (see methods); grey contours denote unstable place cells; cells without contours were not classified as place cells. Scale bar: 100 μm.

c. Place fields along the linearised trajectory, sorted by place cell identity at each imaging stage.

d. Same as **c.** but for unstable place cells at each imaging stage.

e. Left: proportion of stable place cells relative to the number of total recorded cells. Right: proportion of stable place cells relative to the number of total place cells identified at each individual stage.

f. Tuning curve (TC) correlations for stable place cells between imaging stages (stage1-3; stage1-2; stage 2-3).

g. Trial-to-trial TC correlations, in-field to out-field selectivity and in-field peak activity for stable place cells at each imaging stage.

h. Same as **g.** but for unstable place cells.

Data are presented as mean ± s.e.m. Control group: stable place cells, n = 170; unstable place cells, n = 774, 886, and 945 at each stage; 10 imaging sessions from 5 mice per stage. 5xFAD group: stable place cells, n = 162; unstable place cells, n = 669, 814, and 732 at each stage; 7 imaging sessions from 4 mice per stage. Statistical comparisons were made using two-sided Wilcoxon rank-sum tests with Holm–Bonferroni correction for multiple comparisons.

291 **4. Weakened contextual representations in CA1 trajectory-dependent encoding**

292 A splitter cell is a neuron whose activity on a shared path (here, the stem arm of maze)
293 varies depending on the animal's trajectory. Splitter cells are thought to encode task-
294 relevant contextual information and contribute to flexible memory-guided behaviour [37, 38].
295 To identify splitter cells, we examined neuron with a place field spanning at least five
296 spatial bins along the stem arm and exhibiting trajectory-dependent activity during left
297 and right-turn trials (Fig. 4a; Methods). For each neuron, spatial tuning curves were
298 constructed separately for correct left-right (LR) and right-left (RL) trials. Trajectories were
299 classified as high-rate or low-rate based on which turn direction produced the higher peak
300 spatial activity on the stem arm (Fig. 4b). Splitter cells were then identified based on
301 significant differences between high- and low-rate tuning curves, and splitting quality was
302 quantified using several metrics (Methods).

303 We found that the spatial tuning calcium activity on the high-rate trajectory was reduced
304 in early-stage 5xFAD mice ($F(1, 14352) = 214.77$, $p < 0.001$; Fig. 4c). The probability that
305 individual stem bin exhibited splitting activity was also decreased in AD mice (Genotype
306 × Spatial bin interaction: $F(15, 14352) = 8.51$, $p < 0.001$; Fig. 4d). Consistently, the
307 proportion of splitter cells was significantly lower in 5xFAD mice compared with controls
308 (Ctrl: 11.9 ± 1.3%; AD: 9.8 ± 2.4%; $p = 0.03$; Fig. 4e).

309

310 Next, we evaluated several metrics of splitting quality. Neither split extent (β =-0.05, 95%
311 CI [-0.12, 0.019], $p = 0.16$; Fig. 4f) nor split discriminability (β = -0.04, 95% CI [-0.10, -

312 0.03], p = 0.30; Fig. 4g) differed significantly between genotypes, although both showed
313 non-significant reduction trends. In contrast, the active split-trial ratio was significantly
314 reduced in 5xFAD mice (β = -0.12, 95% CI [-0.22, -0.007], p = 0.037; Fig. 4h), the onset
315 of splitting activity (first split trial) occurred later (β = 1.63, 95% CI [0.95, 2.32], p < 0.001;
316 Fig. 4i), and trial-to-trial reliability across high-rate trajectories decreased (β = -0.02, 95%
317 CI [-0.04, -0.008], p = 0.004; Fig. 4j). These results suggest that although the basic spatial
318 tuning of splitting activity may remain, its trial-by-trial consistency and engagement are
319 impaired in 5xFAD mice. At the population level, a linear discriminant analysis decoder
320 trained on all stem-active neurons achieved significantly lower decoding accuracy in AD
321 mice (correlation rrb = -0.49, p = 0.021; Fig. 4k), demonstrating impaired trajectory-
322 dependent coding across the network.

323

324 Finally, cross-age correlations between splitter cell quality and behavioural performance
325 further support functional relevance of these neurons (active split-trial ratio: r = 0.50, p =
326 0.008; split extent: r = 0.57, p = 0.002; split discriminability: r = 0.54, p = 0.004;
327 Supplementary Fig. 4). Importantly, in early-stage 5xFAD mice, impairments in splitter cell
328 properties emerged before any observable deficits in task performance in the head-fixed
329 alternation task.

330

331

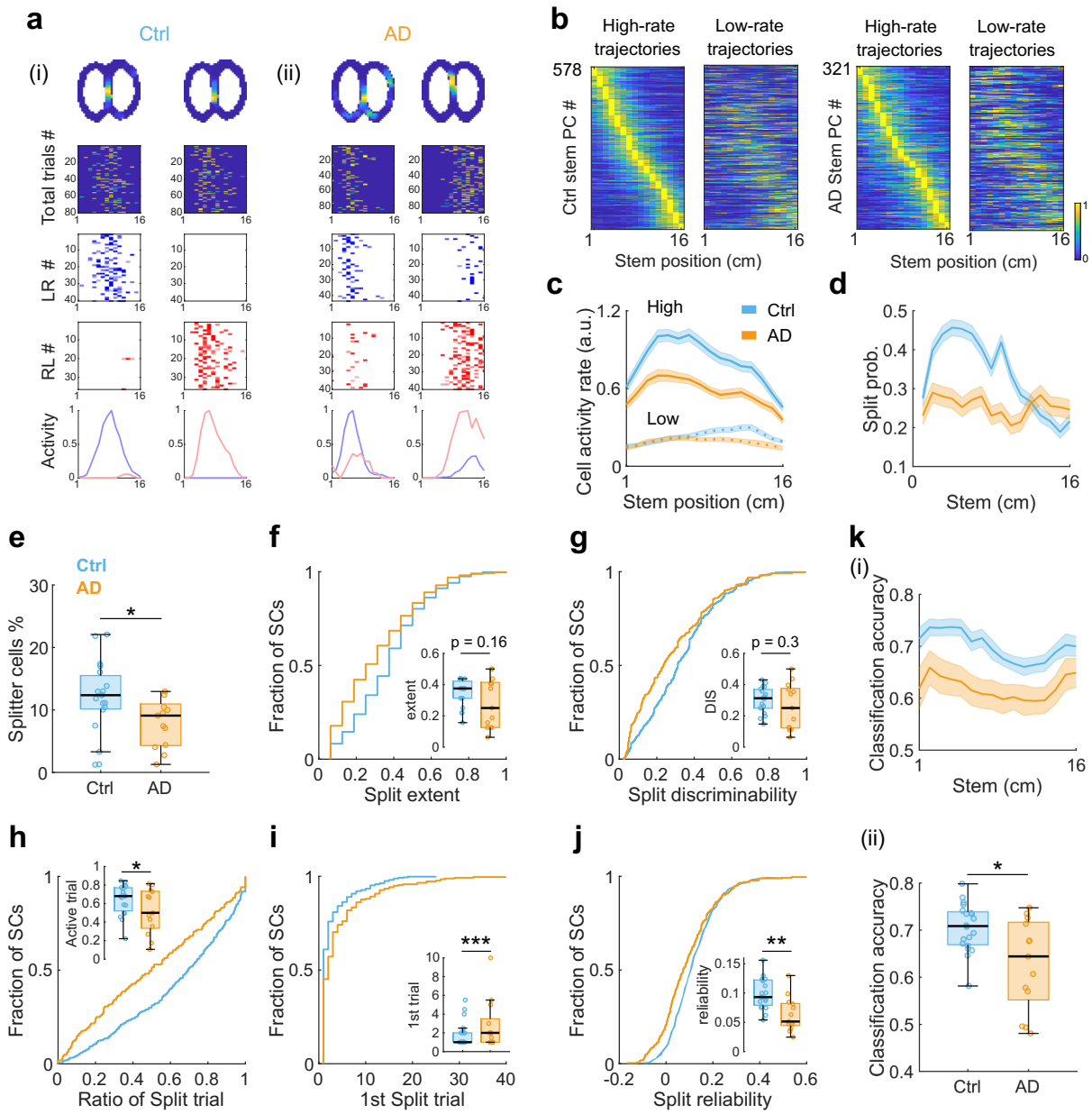

Figure 4: Impaired hippocampal splitting activity in early stage of 5xFAD mice

a. Two representative stem place cells exhibiting splitting activity in control and 5xFAD mice. From top to bottom: normalised two-dimensional calcium activity map for the figure-8 maze from one imaging session; calcium activity raster along the stem for all trials, with the corresponding

337 linearised behavioural profile; calcium activity raster for left–right trials (blue); calcium activity
338 raster for right–left trials (red); normalised calcium tuning curves for each turn direction.

339 **b.** Difference in calcium activity rates between left and right trajectories for CA1 cells with stem
340 place fields. Trajectories were classified as high- or low-rate based on the direction with the higher
341 peak spatial activity rate. Activity was normalised to each cell's peak firing rate and sorted by field
342 position on the high-rate trajectory. Each line represents one cell.

343 **c.** Mean ± s.e.m. spatial activity (from panel b) along the stem for high-rate (solid) and low-rate
344 (dotted) trajectories.

345 **d.** Probability of each stem bin exhibiting splitting activity.

346 **e.** The proportion of splitter cells. one-sided Wilcoxon rank-sum test.

347 **f–j.** Splitting properties of splitter cells:

348 **f.** Proportion of spatial bins showing splitting activity;

349 **g.** Discriminability between high- and low-rate trajectories;

350 **h.** Proportion of trials with activity on the high-rate trajectory;

351 **i.** First trial number exhibiting splitting activity;

352 **j.** Trial-to-trial correlation across adjacent high-rate trajectories.

353 Cumulative plots showed data across all cells, and insert box plot showed the median value of
354 imaging sessions in control and 5xFAD mice. All assessed with linear mixed-effects models.

355 **k.** Decoding accuracy of a discriminant analysis classifier using all stem-active cells. (i) Decoding
356 accuracy along the stem; (ii) median decoding accuracy for each imaging session. Two-sided
357 Wilcoxon rank-sum test.

358 Control: stem place cells, n = 578; splitter cells, n = 521; 20 imaging sessions from 10 mice.
359 5xFAD: stem place cells, n = 321; splitter cells, n = 264; 13 imaging sessions from 7 mice.
360
361
362 **5. Reorganisation of CA1 contextual encoding patterns in early-stage AD mice**
363
364 Given the pronounced impairments in splitter cell activity in early-stage AD-model mice,
365 we next examined whether behavioural choice influenced trajectory-dependent encoding
366 along the stem arm. We focused on CA1 place cells with fields located on the stem and
367 applied an dissimilarity analysis adapted from Varga et al.[39] to determine whether single-
368 trial activity reflected the behavioural context of the past, current, or upcoming turn.
369
370 Error trials are essential for dissociating retrospective from prospective coding [40],
371 analyses were restricted which mice had at least three left error and right error trials. For
372 each spatial bin, we computed dissimilarity of cell activity between two relevant trial types
373 (e.g., LR vs. LL for retrospective; LR vs. RR for prospective; Fig. 5a) and derived a Retro–
374 Pro bias index for each cell (Fig. 5b). Consistent with previous studies [39, 40], most splitter
375 cells in our task exhibited a strong retrospective bias (Fig. 5c).
376
377 Despite intact alternation performance at this age, early-stage 5xFAD mice showed
378 markedly altered distributions of contextual encoding types. The Retro-Pro bias was
379 significantly shifted toward more prospective-biased encoding compared with controls (β
380 = 0.13, 95% CI [0.09, 0.18], $p < 0.001$; Fig. 5d). Retrospective encoding was diminished,

while prospective encoding was enhanced in early-stage AD mice, leading to this increased Retro-Pro bias during trajectory-dependent contextual coding (Supplementary Fig. 5). Furthermore, control mice gradually transitioned toward prospective encoding only when approaching the choice point, but AD mice displayed an earlier and stronger shift to prospective encoding along the stem (Genotype × spatial bin interaction: $F(15, 8779) = 2.29$, $p = 0.003$; two-way ANOVA; Fig. 5e). This pattern reveals a marked reorganisation of trajectory-dependent contextual coding in early-stage AD mice, reflected in a shift from retrospective towards more prospective encoding.

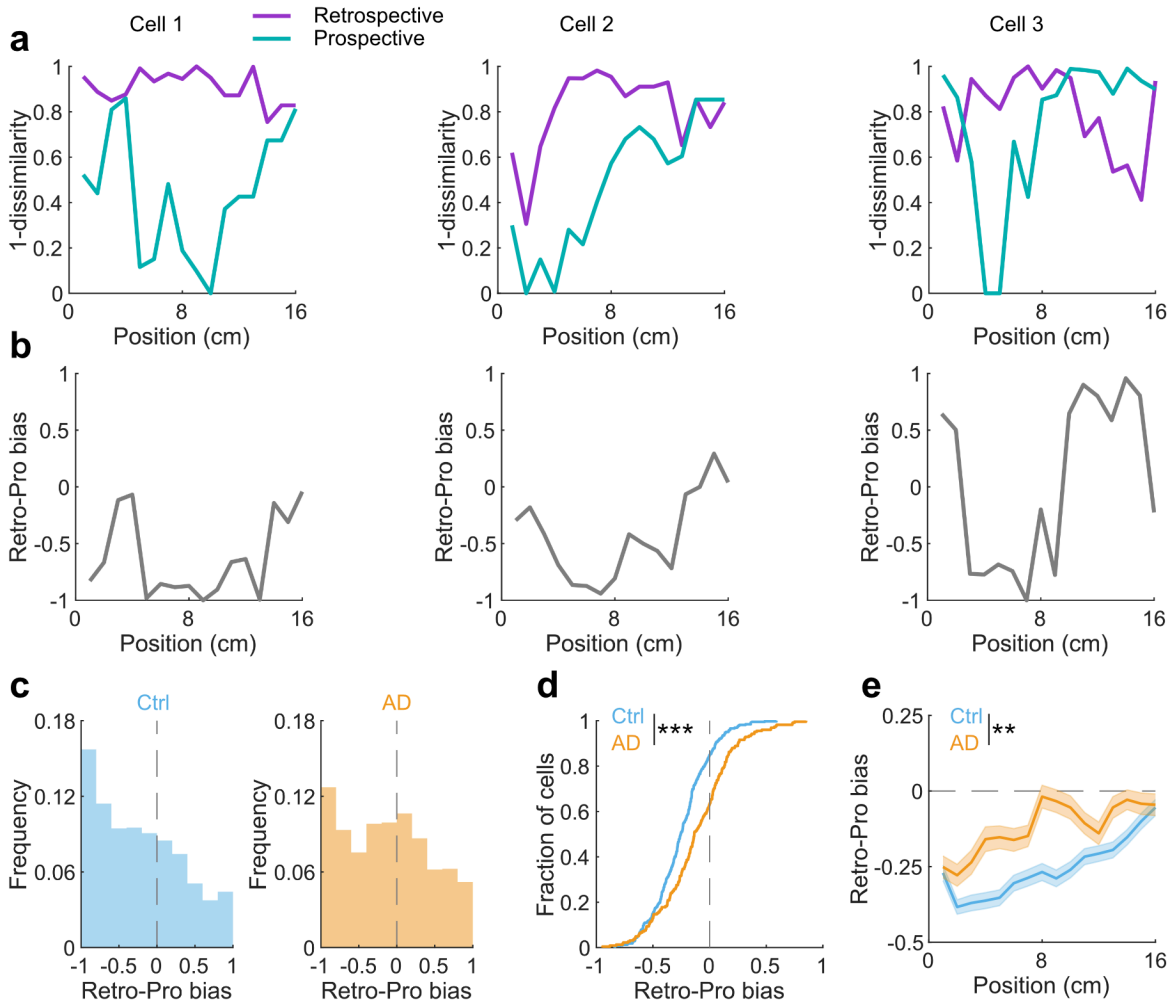

Figure 5. Altered hippocampal trajectory encoding patterns in early-stage AD mice.

a. The 1 − (normalized dissimilarity) values for retrospective and prospective encoding are shown for three example stem arm place cells. Dissimilarity was computed as −log10(p value$_{\text{(Wilcoxon rank-sum test)}}$) of cell activity at each spatial bin between two trial types (e.g., LR vs. LL for retrospective encoding; LR vs. RR for prospective encoding); higher dissimilarity indicates greater differences between trial types.

400 **b.** Retro–Pro bias index along stem arm of the cell in panel **a**, ranging from −1 (purely
401 retrospective encoding) to 1 (purely prospective encoding).

402 **c.** Histogram distribution of Retro–Pro bias values in control and AD mice. Most cells in control
403 mice exhibited a retrospective bias.

404 **d.** Average Retro–Pro bias across stem spatial bins for each cell.

405 **e.** Retro–Pro bias along the stem arm (16–0 cm toward the choice point). Shaded regions indicate
406 mean ± s.e.m. across cells. Genotype × spatial bin interaction: $p = 0.003$, two-way ANOVA test;

407 Ctrl: n = 384 splitter cells from 10 imaging sessions (5 mice). AD: n = 225 splitter cells from 7
408 imaging sessions (4 mice).

409

410

411 **6. Basal forebrain cholinergic activation improved CA1 coding in early-stage**
412 **5xFAD mice**

413

414 Previous studies have shown that medial septal cholinergic neurons play a key role in
415 enhancing hippocampal theta oscillations during exploration[41]. We therefore examined
416 whether activating these neurons could enhance spatial and contextual coding in
417 hippocampal CA1 and mitigate early deficits in 5xFAD mice. To achieve selective
418 activation, AAV-hSyn-DIO-hM3D(Gq)-mCherry was injected into the medial septum of
419 ChAT-Cre^{+}/5xFAD^{+} (AD) and ChAT-Cre^{+}/5xFAD^{-} (control) mice, and AAV-syn-
420 jGCaMP7s was injected in dorsal CA1. A cranial window was then implanted for in vivo

421 calcium imaging (Fig. 6a). After all mice reached the task acquisition criterion, vehicle
422 (saline) was administered intraperitoneally on the first imaging day and CNO on the
423 second imaging day. CNO administration did not alter behavioural alternation
424 performance and locomotion in either group (Ctrl: $p = 0.81$; AD: $p = 0.64$; two-sided
425 Wilcoxon signed-rank test; Fig. 6b, Supplementary Fig. 6a,b).

426

427 Tracking the same neuronal populations across vehicle and CNO sessions, we observed
428 increased global spatial information (computed from two-dimensional spatial firing maps)
429 following CNO administration in both control ($\beta = 0.37$, 95% CI [0.13, 0.61], $p = 0.002$)
430 and 5xFAD mice ($\beta = 0.30$, 95% CI [0.06, 0.54], $p = 0.013$). Similarly, place cell spatial
431 information during correct trials increased in both groups (Ctrl: $\beta = 0.12$, 95% CI [0.008,
432 0.23], $p = 0.036$; AD: $\beta = 0.19$, 95% CI [0.06, 0.32], $p = 0.005$). In 5xFAD mice, this was
433 accompanied by a significant increase in trial-to-trial TC correlation of place cells following
434 CNO administration ($\beta = 0.02$, 95% CI [0.004, 0.036], $p = 0.015$; Fig. 6e,f), whereas
435 control mice showed no such change ($\beta = 0.00$, 95% CI [-0.01, 0.01], $p = 0.95$). However,
436 CNO treatment did not rescue place cell in-field selectivity or peak in-field activity in
437 5xFAD mice (Supplementary Fig. 7b-d), although we observed a reduction in place field
438 size in control mice after CNO (Supplementary Fig. 6e).

439

440 We next assessed trajectory-dependent activity in stem place cells. Mirroring the
441 improvements observed in place cells, the ratio of trials in which stem place cells
442 displayed trajectory-dependent coding increased significantly in 5xFAD mice after CNO

443 administration (β = 0.15, 95% CI [0.05, 0.26], p = 0.003; Fig. 6g). Moreover, the first-trial
444 onset of splitting activity exhibited a trend towards earlier emergence in 5xFAD mice (β =
445 -1.25, 95% CI [-2.50, 0], p = 0.050; Fig. 6h), whereas no significant changes were
446 observed in control mice (splitting extent: β = -0.04, 95% CI [-0.11, 0.036], p = 0.32; first
447 split trial: β = -0.02, 95% CI [-1.46, 1.40], p = 0.97). Other metrics of trajectory-dependent
448 activity, including extent, reliability, and discriminability, were unaffected by CNO in
449 5xFAD mice (Supplementary Fig. 6g-i).

450

451 Together, these findings suggest that chemogenetic activation of medial septal
452 cholinergic neurons enhances the spatial representations and promotes trajectory-
453 dependent coding in CA1, thereby increasing trial-wise stability in early-stage 5xFAD
454 mice (Supplementary Fig. 6j), although the rescue remains partial and does not extend
455 to all dimensions of hippocampal coding.

456

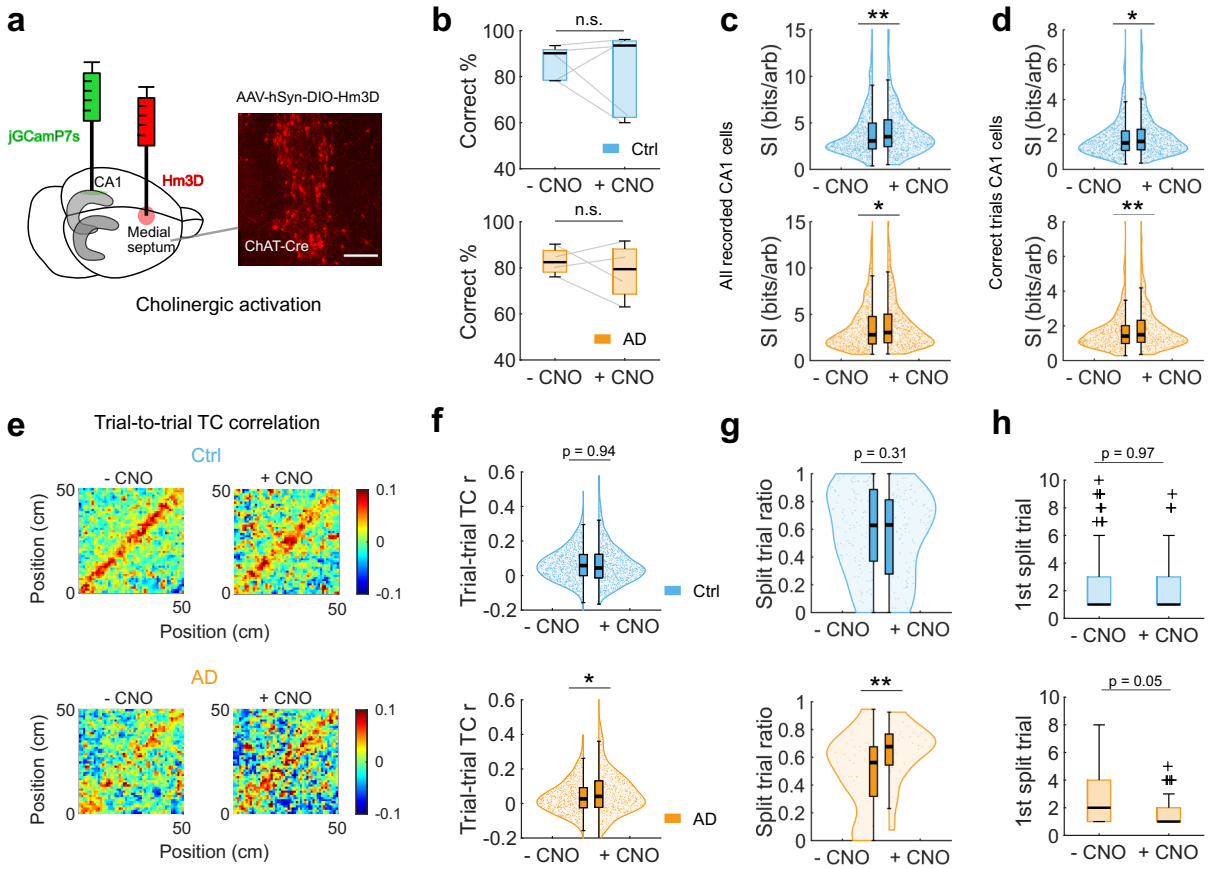

Figure 6. Basal forebrain cholinergic activation modulated CA1 spatial and contextual coding in early-stage 5xFAD mice

a. Experimental schematic showing DREADD (hM3Dq) expression in medial septal cholinergic neurons of the basal forebrain and jGCaMP7s expression in hippocampal CA1. Right: representative image of hM3Dq expression in ChAT-Cre mice. Scale bar, 100 μm. **b.** Performance in a spontaneous alternation task following intraperitoneal (i.p.) injection of saline (vehicle) or clozapine-N-oxide (CNO); Wilcoxon signed-rank test.

c. Global spatial information (from two-dimensional spatial firing maps) of all CA1 neurons after vehicle or CNO administration.

468 **d.** Spatial information of CA1 place cells during correct trials following vehicle or CNO treatment.
469 **e.** Trial-to-trial tuning curve correlations of CA1 place cells during correct trials under vehicle or
470 CNO conditions.
471 **f.** Mean diagonal Pearson correlation coefficients of CA1 place cells from (**e**).
472 **g**. The proportion of trials in which stem place cells displayed trajectory-dependent coding.
473 **h.** Latency to the first trial exhibiting trajectory-dependent activity in stem place cells. For clarity,
474 outliers >10 are not shown in figure.
475 Data were analysed using linear mixed-effects models with treatment group (CNO vs vehicle) as
476 a fixed effect and Mouse ID as a random intercept. Ctrl: 964 detected neurons; place cells: 697
477 (140 stem place cells) after vehicle, and 522 (122 stem place cells) after CNO; 5 mice. AD: 777
478 detected neurons; place cells: 522 (46 stem place cells) after vehicle, and 449 (41 stem place
479 cells) after CNO; 4 mice.

480

481 **Discussion**

482 In this study, we introduced a novel head-fixed behavioural paradigm to assess
483 hippocampal-associated spatial memory. This paradigm allowed us to examine
484 behavioural performance and hippocampal neuronal spatial representations by two-
485 photon in vivo imaging in 5xFAD mice during a continuous spatial alternation task (Fig.
486 1a, b). Previous research has established that the 5xFAD mouse begins to develop
487 amyloid deposits between 2 to 4 months of age, with intraneuronal accumulation of Aβ42
488 starting as early as 1.5 months [29] . This amyloid burden in 5xFAD mice intensifies over
489 their lifespan [29, 42]. By 4 to 6 months, these mice exhibit substantial amyloid deposition
490 alongside observed deficits in synaptic transmission, LTP, and sharp wave-ripple events
491 [26, 29, 33, 43]. While some studies have detected mild impairments in spatial or hippocampus
492 independent memory as early as 3 to 4 months, more pronounced memory deficits
493 become evident at later stages, beyond 4-6 months of age [27, 44, 45, 46]. Consistent with
494 these findings, our study observed intact behavioural performance in young 5xFAD mice
495 (2-4 months) during the head-fixed alternation task (Fig. 1c-e), and substantial
496 behavioural impairments emerged only after ~7 months of age in 5xFAD mice (Fig. 1f–h).

497

498 Disruptions in hippocampal spatial representations have been reported in both human
499 sporadic AD and multiple AD mouse models [47, 48]. In our study, although 2-4 month-old
500 5xFAD mice exhibited normal performance in the spatial alternation task (Fig. 1c–e), their
501 CA1 neurons showed clear impairments in spatial coding, including reduced spatial

502 information and decreased stability at both the population level and in task-related place
503 cells (Fig. 2). Interestingly, global spatial representations were preserved, yet task-related
504 spatial coding was impaired, suggesting that behavioural demands reveal spatial
505 information deficits that are more vulnerable at the global level. Notably, a previous report
506 using 3-5 month-old APP-KI mice found intact CA1 spatial tuning and remapping despite
507 the presence of amyloid plaques [49]. These differences may reflect model-specific
508 progression of pathology or the fact that our task is strongly goal-directed, which places
509 greater demands on task relevant place cell coding.

510

511 The stabilisation of place cell coding is closely linked to the memory demands and
512 attentional engagement required in goal-directed tasks [50, 51]. In our task, stable place cells
513 in early-stage 5xFAD mice continued to exhibit consistent spatial tuning across learning
514 stages (Fig. 3c, e-g). Previous work has shown that more excitable neurons tend to
515 maintain stable spatial representations across days [52], and that stable place cells
516 accumulate during learning correlate strongly with behavioural performance in healthy
517 mice [53] . Thus, the preserved quality of stable place cells in young 5xFAD mice may help
518 maintain long-term spatial memory across repeated training in a familiar environment,
519 thereby supporting intact performance in the spatial alternation task. In contrast, CA1
520 population activity showed reduced flexibility: PV correlations across learning stages were
521 higher in 5xFAD mice (Supplementary Fig. 3b), indicating diminished population-level
522 remapping and a more rigid representational structure across task learning. Together,
523 these results suggest that although broader CA1 coding is destabilised in early-stage AD,

524 a preserved subset of stable place cells may provide sufficient representational continuity
525 to sustain behaviour.

526

527 Recent work suggests that the hippocampus supports cognitive processes beyond spatial
528 mapping [54, 55, 56]. Our findings extend this view by demonstrating impairments in both
529 spatial and contextual representations within the same behavioural framework. Splitter
530 cells, which encode past choices and future behavioural outcomes, are thought to
531 integrate information within prefrontal-thalamo-hippocampal circuits that guide flexible
532 navigation [38]. Trajectory-dependent coding was markedly degraded, at populational level
533 and single cell level at early-stage of AD (Fig. 4). Although the splitting extent and
534 discriminability were preserved in 5xFAD mice, the trial-trial engagement and stability of
535 splitting activity were reduced and closely associated with behavioural deficits (Fig. 4e-
536 j;Supplementary Fig. 4). Notably, while the proportion of place cells showed a mild, non-
537 significant reduction, the proportion of splitter cells was significantly diminished, indicating
538 that trajectory-dependent representations are more vulnerable than spatial encoding at
539 early stages of AD.

540

541 We found that most splitter cells preferentially encoded retrospective rather than
542 prospective information in our task (Fig. 5c,d), indicating that neuronal activity along the
543 common stem was dominated by information about the past choice. This retrospective-
544 prospective balance became more even only when mice approached the choice point
545 (Fig. 5c,d). The earlier and stronger shift toward prospective coding observed in 5xFAD

546 mice may reflect weakened maintenance of past information before the next decision,
547 potentially linked to reduced hippocampal-prefrontal synchrony reported in 5xFAD mice
548 [57]. Previous studies have similarly shown that splitter cells typically favour retrospective
549 encoding, and our results are consistent with this pattern. However, the stronger
550 retrospective bias near the choice point in our task may be influenced by the shorter stem
551 length compared with earlier studies [39, 40].

552

553 A reduction in trial-to-trial stability was evident in both spatial and contextual
554 representations, suggesting that early coding deficits in CA1 may reflect a common
555 disturbance affecting representational consistency. These spatial and contextual coding
556 impairments may link with known synaptic disturbances in 5xFAD mice, including reduced
557 long-term potentiation (LTP) and impaired synaptic transmission from early age [17, 26, 43,
558 58]. Changes in CA1 representations across learning rely heavily on synaptic plasticity
559 driven by inputs from entorhinal cortex layer 3 [59]. The emergence of splitter cells likely
560 requires the recruitment of more complex and highly integrated neural networks, as well
561 as stronger plasticity mechanisms. Given that synaptic plasticity can convert previously
562 silent CA1 neurons into splitter cells [23], early synaptic impairments may therefore
563 contribute to deficits in both spatial and contextual representations observed in 5xFAD
564 mice.

565

566 Chemogenetic activation of medial septal cholinergic neurons enhanced spatial
567 information and increased the trial-wise engagement of spatial and contextual encoding

568 in early-stage 5xFAD mice (Fig. 6). This system is known to be compromised in AD, and
569 cholinergic decline has been linked to cognitive deterioration in several
570 neurodegenerative conditions[60, 61, 62]. Basal forebrain cholinergic neurons send dense
571 projections to the hippocampus and play a central role in regulating hippocampal synaptic
572 plasticity, learning and memory[28]. Cholinergic activity also promotes hippocampal theta
573 oscillations, which support spatial coding and memory-guided behaviour [63]. In 5xFAD
574 mice, the basal forebrain is the first brain region to show cholinergic neuron loss,
575 beginning to degenerate from around nine months of age, which indicates an early
576 vulnerability of this system [64]. Although Alzheimer's disease remains incurable, several
577 approved treatments, including donepezil, galantamine and rivastigmine, act as
578 cholinesterase inhibitors and increase acetylcholine levels. These observations suggest
579 that targeting basal forebrain cholinergic neurons may still offer a promising strategy for
580 early intervention in AD.

581

582 Early tetrode studies were limited by the small number of neurons that could be recorded
583 simultaneously, whereas two-photon imaging in virtual-reality environments, although
584 scalable, lacks the multimodal sensory cues that shape place-cell activity [65, 66]. More
585 recent real-world head-fixed mazes address some of these constraints [67] , yet most
586 imaging studies still use relatively simple running tasks. Because such tasks place limited
587 cognitive demands on the animal, they may not fully reveal the types of representational
588 deficits relevant to AD. This study integrates a real-world environment with a cognitively

589 demanding alternation task to investigate hippocampal function in early-stage AD,
590 providing insights under behaviourally relevant context.

591

592 **Limitations of the study**

593 First, we did not account for sex differences in our analysis. Human studies indicate that
594 AD prevalence and severity are higher in females, with sex-specific differences observed
595 in amyloid pathology and cognitive decline [68, 69]. Similar patterns have been reported in
596 the 5xFAD model, with female mice exhibiting greater amyloid deposition and potentially
597 distinct cognitive impairments compared to males [70, 71, 72, 73]. Second, although calcium
598 imaging is a powerful tool for assessing neuronal activity, potential discrepancies in
599 calcium indicator dynamics in AD models must be considered. Variations in calcium
600 indicator expression, deregulation of calcium signalling, and altered decay kinetics in
601 5xFAD mice could affect the accuracy of spike inference [74]. Third, incorporating pupil and
602 lick tracking could provide further insights into attention and task engagement, thereby
603 clarifying the mechanisms underlying the observed behavioural impairment. Finally, our
604 behavioural assessment was limited to a single task that lacked an explicit delay period,
605 relying instead on the animal's natural return time to the choice point. Incorporating a
606 controlled delay (such as with a servomotor gate) could increase the task's reliance on
607 intrinsic hippocampal processing, as suggested by studies in freely moving animals, but
608 was beyond the scope of the present work [37].

609

610

611 **Materials and Methods**

612

613 **Experimental Animals:**

614 5xFAD mice express human APP and PSEN1 transgenes with a total of five AD-linked
615 mutations: the Swedish (K670N/M671L), Florida (I716V), and London (V717I) mutations
616 in APP, and the M146L and L286V mutations in PSEN1. Male hemizygous 5xFAD mice
617 (B6SJL-Tg (APPSwFILon, PSEN1∗M146L∗L286V) 6799Vas/Mmjax, JAX stock #
618 034840) were crossed with female homozygous Chat-IRES-Cre(△neo) mice (JAX stock
619 # 031661 on a C57BL/6J genetic background) to maintain the 5xFAD positive
620 ($5xFAD^+$/Chat-Cre^+ as 5xFAD group) and non-5xFAD ($5xFAD^-$/Chat-Cre^+ as control
621 group) mice. Colonies under standard animal breeding at Imperial College London. The
622 animal room was kept on a reverse 12:12 light-dark cycle daily.

623

624 Ear samples were collected from 5xFAD-Tg and Non-5xFAD-Tg transgenic littermates for
625 genotyping identification. Real-time PCR was used for genotyping 5xFAD transgenic with
626 probes APPswTg and huPSEN1Tg, conducted by Transnetyx. Animals were divided into
627 two age groups: young group aged (young control median age = 3.6 months, N=10; young
628 AD median age = 3.6 months, N=7) and old group aged (old control median age = 8.6
629 months, N=6, old AD median age = 7.9 months, N=6). Non-AD transgenic littermates were
630 used as controls. Both male and female mice were used for this study. All experimental
631 procedures were carried out under the Animals (Scientific Procedures) Act 1986 and
632 according to Home Office and institutional guidelines, under a Project License to SR

633 Schultz.

634

635 **Surgeries:**

636 Mice were anaesthetised with 1.5-3% isoflurane (Iso-Vet, Chanelle Pharma) and body
637 temperature was maintained at 37°C. Analgesia was administered pre-operatively with
638 Carprofen (5 mg/kg SC, Rimadyl, Zoetis) and Buprenorphine (0.07 mg/kg SC, Vetergesic,
639 Ceva Animal Health Ltd). Anaesthetic depth was monitored every 10 minutes via the
640 pedal flexion reflex. A small (0.5 mm) craniotomy was performed and 1 µl of a viral cocktail
641 containing two adeno-associated viruses (pGP-AAV-syn-jGCaMP7s-WPRE, Addgene
642 catalogue 104487-AAV9; pAAV-CAG-tdTomato, Addgene catalogue 59462-AAV9) in a
643 3:1 ratio was injected into the hippocampal CA1 region (coordinates from bregma, in mm:
644 -1.3 and -1.5 DV, -1.8 ML, -2.0 AP). Ten minutes after viral injection, a 3-mm circular
645 craniotomy was made, and the overlying cortex (including parietal cortex and parts of
646 visual and hindlimb sensory cortex) was aspirated using a 27-gauge needle connected to
647 a water pump until the corpus callosum fibres were exposed. A stainless-steel cannula (3
648 mm diameter, 1.5mm height) with a glass bottom was inserted and secured with histoacryl
649 glue (B. Braun Surgical). The hippocampal imaging window was described by Dombeck
650 et al. [75]. A stainless-steel head plate (8.5 mm aperture) was glued to the skull, centred
651 over the craniotomy. The exposed skull outside the head plate aperture was covered with
652 dental cement mixed with black powder paint. Postoperatively, mice received Carprofen
653 (5 mg/kg/24 hrs) in oral water for three days. Behavioural training began after a 2-3 week
654 recovery period.

655

656

657 **Behavioural training in head-fixed mice**

658

659 **Maze apparatus:**

660 We used a carbon fibre maze with attached visual and tactile cues, floating on the
661 Neurotar tracker air table (Mobile HomeCage, Neurotar). Built-in magnets in maze
662 allowed for tracking the animal's position within the environment. The maze has a
663 diameter of 32.5 cm, with a 16 cm-long stem arm. The corridor width for all arms was 5
664 cm. Visual cues were provided by attached phosphorescent tape, and tactile cues were
665 added using Fiberglass Mesh Tape on the inner wall of the maze. The training cage tape
666 was fully charged with daylight before the commencement of any training sessions.

667

668 **Handling and habituation:**

669 Acclimatization to both the room and maze is essential for mice to become familiar with
670 the training environment prior to official training sessions. Mice were handled at least two
671 days before behavioural training. On the day before training began, mice freely explored
672 the air-lifted T maze in the training room under red lighting for 10 minutes. During the first
673 5 training days, mice were allowed 5 minutes of free exploration before head fixation.

674

675 **Spatial continuous rewarded alternation task:**

676 To motivate task engagement, mice were subjected to water restriction prior to the first
677 day of training. After 5 days, their body weight typically stabilised at 85 to 90% of initial
678 body weight, with each mouse receiving a minimum of 1.5 ml of water per day. If the full

679 daily water ration was not received during the task training, supplementary water was
680 provided in the home cage after the second session to maintain body weight above 85%.
681 Mice were trained in the dark during the learning of the alternation task. For the first trial,
682 mice could freely choose reward arm. A 4 μl reward was delivered via a lick spout
683 attached to the head-plate clamp and controlled by a peristaltic pump (Campden
684 Instruments), accompanied by a beep. In subsequent trials, a reward was only delivered
685 when mouse entered the reward arm opposite to the one visited in the previous trial. A
686 complete trial required the mouse to pass through the previous trial reward position, return
687 arm, stem arm, choice arm, and arrive at the next reward location. Head-fixed animals
688 were trained for 45 minutes each session twice a day, with at least 4 hours between
689 sessions. From the 6th training day onward, 1% sucrose water was used as the reward
690 during training and imaging sessions, but still supplied water for supplementary fluid.
691 Mouse position and behavioural data were recorded using the Neurotar Mobile
692 HomeCage tracker (V3.0.0.64). The figure-8 maze was cleaned with 70% ethanol before
693 each mouse training or imaging recording.

694

695 **In vivo two-photon Ca2+ imaging:**

696 Two-photon calcium imaging was conducted using a Scientifica resonant scanning
697 microscope with a 16× Nikon water-immersion objective (LWD 0.8 NA). jGCamp7s and
698 tdTomato fluorophores were excited at 940 nm using Ti:Sapphire laser (Mai Tai HP,
699 Newport). The 50% (vol%) ultrasound gel was used as the immersion medium. Images
700 (490 × 490 μm, 512 × 512 pixels) were acquired at 30.9 Hz frame rate using SciScan 1.3

701 software. Imaging was synchronized with behaviour recording via a start TTL signal sent
702 from the behaviour recording software Neurotar. All mice underwent imaging afterwards
703 10th training day. Additionally, some mice were also imaged on 6th and 8th training
704 days to enable imaging across the learning period. Each imaging session lasted no longer
705 than two hours per mouse per day. At the beginning of each session, mice were head-
706 fixed at the stem arm and restricted by two carbon fibre doors. Once the targeted field of
707 view (FOV) was located, the doors were removed and imaging commenced as the mouse
708 began running. To ensure sufficient data for spatial tuning analyses, a minimum of 80
709 total trials was required for each imaging session, though approximately 100 trials were
710 usually recorded per session.

711

712 **Chemogenetic activation**

713

714 For chemogenetic activation of basal forebrain cholinergic neurons, 0.5–1.0 μL AAV-
715 hSyn-DIO-hM3D(Gq)-mCherry was injected into the medial septum (AP +0.8 mm, ML
716 +0.1 mm, DV −4.2 to −4.0 mm from bregma), and jGCaMP7s was delivered into dorsal
717 hippocampal CA1. DREADDs experiments were performed only after mice reached
718 stable task performance. Animals were recorded across two consecutive imaging days.
719 On the first day, mice received an intraperitoneal injection of saline (vehicle). On the
720 second day, Clozapine-N-oxide (CNO; 1 mg/kg, i.p.; water-soluble CNO dihydrochloride,
721 HelloBio HB6149) was administered 40 minutes before imaging. A low CNO dose was
722 used to minimise off-target effects, and previous studies have reported that 1 mg/kg CNO

723 does not alter hippocampal neuronal activity without hM3D injection in ChAT-Cre mice [76].
724 The same neuronal population was tracked across vehicle and CNO sessions.
725
726
727 **Quantification and statistical analysis**
728
729 **Behaviour data analysis:**
730 Only complete trials (see behaviour training) were included in the analysis. As mice
731 received a reward on their initial free choice, this first choice was excluded from the
732 calculation of correct trials. Alternation performance was defined as the percentage of
733 correct trials out of the total number of trials. To examine changes in performance across
734 training days, we fitted a linear mixed-effects model (LMM): data ~ 1 + Genotype × Day
735 + (1 | MouseID). Performance (percentage of correct trials) was the dependent variable.
736 The model included Genotype (5xFAD, Control), Training days (as a continuous
737 numerical predictor), and their interaction as fixed effects. To account for repeated
738 measures from the same subject, Mouse ID was included as a random intercept. To
739 further assess learning dynamics independent of daily variability, trials from all sessions
740 were concatenated and binned into consecutive 50-trial blocks, with the percentage of
741 correct responses computed for each block. Learning trajectories across groups were
742 then modelled using a quadratic mixed-effects model: Performance ~ Genotype × (Block
743 + Block^2) + (1|MouseID). Differences in task learning performance between 5xFAD mice
744 and their age-matched controls were determined based on the Genotype × Day and

745 Genotype × Block interaction effects. Task acquisition criterion is the percentage of
746 correct trials is over 70% over four consecutive trial blcoks.
747
748 **Trajectory linearisation:**
749 To linearise the mouse trajectory, the maze was segmented into four functional zones:
750 the return arm, stem arm, choice arm and reward arm. Trajectories were parsed
751 accordingly, starting from the return arm, then moving up the stem arm into the choice
752 arm, and ending in the reward arm. The reward spout marked the boundary between the
753 choice and reward arms. Each trajectory was then categorised into L-R, R-L, L-L and R-
754 R trial types based on maze segmentation. Linearised trajectories were mapped by trial
755 type onto a standardised 49.5 cm track, corresponding to the estimated length of a
756 complete trial. Trials were chronologically ordered based on the sequence of completion
757 in the maze.
758
759 **Imaging data processing:**
760 To extract calcium activity from individual neurons, we employed a customised image
761 processing pipeline based on the CaImAn MATLAB package [77], following the protocol
762 described by Go et al. [67]. Imaging data were initially corrected for motion artefacts using
763 sequential rigid and non-rigid registration methods, aligning frames a reference template
764 from the same imaging session. Regions of interest (ROIs) were then identified, with
765 excluding any overlapping ROIs. To enable tracking of ROIs across multiple imaging
766 stages, images from different stages were registered to a template from one session, and
767 ROIs were identified on a temporally concatenated video. For quantification of single-

neuron calcium amplitude trains, neural activity was deconvolved using a sparse non-negative deconvolution approach. This was implemented with an exponential kernel corresponding to the decay timescale of the calcium indicator employed, utilizing the OASIS (Online Active Set method to Infer Spikes) algorithm to infer fluorescence activity into calcium trains with both onset times and amplitudes.

To eliminate out any discrepancies in OASIS event amplitude between different mice and FOVs, we fitted the distribution of event amplitudes for each FOV in each mouse to a lognormal distribution and standardised the distribution for each FOV to unit mean. This eliminates variability in event amplitude due to differences in signal to noise ratio (for instance due to imaging depth and viral expression), and makes it possible to compare calcium activity rates objectively across FOVs and animals. The resulting deconvolved calcium event amplitudes are expressed in consistent arbitrary units across the entire dataset.

Spatial information:

To quantify spatial representations in CA1 neurons, spatial information was calculated from two-dimensional spatial rate maps for each detected neuron. The figure-8 maze was discretised into 1 cm-wide bins, forming a 32 × 32 spatial grid. For each bin, the spatial activity rate was computed as the sum of standardised deconvolved calcium amplitudes recorded within that bin, divided by the total occupancy time, considering only periods when the mouse's running speed exceeded 8 mm/s. The resulting spatial rate maps were smoothed using a Gaussian kernel with a sigma of [3, 3]. The spatial information content

791 of each neuron was calculated using Skaggs's spatial information method [78] (bits per arb,
792 standardised amplitude rate), is calculated using the following formula:

793 $$SI = \sum_{i=1}^{N} P_i \frac{\lambda_i}{\lambda} \log_2 \left(\frac{\lambda_i}{\lambda}\right)$$

794

795 where SI is the spatial information in bits/arb. P_i is the probability of the mouse being in
796 the i-th bin. λ_i is the mean standardised amplitude rate of the cell when the mouse in the
797 i-th bin. λ is the overall mean standardised amplitude rate of the cell across the entire
798 environment. N is the total number of spatial bins.

799

800 **Population vector correlation:**

801 To assess the stability of spatial representations at populational level, we calculated
802 population vector (PV) correlations between odd and even trials. For each session, we
803 first constructed spatially binned activity curves for all detected cells. The population
804 vector at each spatial bin was defined as a vector containing the calcium activity rates of
805 all cells within that bin. We then computed the PV correlation matrix by comparing
806 population vectors between odd and even trials across all spatial bins by Pearson
807 correlation. The diagonal elements of this matrix represent the correlation coefficients for
808 the same spatial positions between trial types, reflecting the stability of spatial coding
809 along the linearized trajectory. Finally, we averaged the diagonal PV correlation
810 coefficients across animals within each experimental group.

811

812 **Place cell identification:**

813 Place cells from two-dimension spatial maps were identified based on the following
814 criteria: 1) A neuron's SI must exceed the 95th percentile of the shuffled SI values. 2) the
815 neuron should be active within the place field for more than 2% of the time the mouse
816 spends in that field. 3) the size of the place field must exceed 5 cm^2. The boundary of a
817 place field was determined by encompassing all connected occupancy bins where was
818 at least 50% of the peak rate in the occupancy bin.
819
820 For place cells selection from one-dimension spatial maps, we calculated for correct trials
821 (R-L and L-R) and error trials (L-L and R-R) based on same type of linearised trajactory.
822 The criterions for 1D place cells : 1) A neuron's SI must exceed the 95th percentile of the
823 shuffled SI values. 2) the neuron should be active within the place field for more than 1%
824 of the time the mouse spends in that field. 3) the neuron were active more than 30% of
825 total number of trials.
826
827 **Place cell quality metrics:**
828 In-field selectivity: the in-field and out-of-field activity rates were computed and
829 normalized by the number of spatial bins. Selectivity was defined as (In-field – Out-
830 field)/(In-field + Out-field). ranging from −1 (purely out-of-field firing) to 1 (purely in-field
831 firing). Peak in-field activity: the maximum activity value within each place field,
832 determined by the spatial bin with the highest activity rate. We also computed: Active trial
833 ratio (Supplementary figure 2): the proportion of trials of the same trajectory type (i.e. left-
834 to-right, or right-to-left) in which a given place cell was active. Adjacent trial-to-trial
835 reliability: for each trial, the spatial activity profile of the neuron was constructed by binning

836 calcium activity along linearised trajectory. Pairwise Pearson correlations were then
837 computed between adjacent active trials of the same trajectory type. The trial-to-trial
838 reliability of each neuron was defined as the mean of these correlation coefficients across
839 all active trial pairs.(for place cells have multiple place field, the PF selectivity and infield
840 peak was computed on the average of the multiple place field)
841
842 **Trial-to-Trial Tuning curve (TC) correlation:**
843 For each identified place cell, we computed trial-to-trial tuning curve correlations to
844 quantify response reliability. Single-trial tuning curves were constructed based on
845 spatially binned calcium activity. Trials were divided into odd and even subsets, and
846 Pearson correlations were calculated between corresponding spatial bins across these
847 trial groups. The resulting correlation matrix's diagonal elements, representing reliability
848 at same spatial positions, were averaged to obtain a single stability metric per cell.
849
850 **Tuning curve (TC) correlation across stages:**
851 TC correlations were computed only for neurons classified as place cells. For each
852 imaging stage, spatially binned activity along the linearised trajectory was constructed for
853 every place cell. TC correlations between stages were calculated using Pearson's
854 correlation coefficient. For stage-1 correlations, tuning curves were generated separately
855 from odd and even trials within the same stage, and the correlation between these two
856 curves was used as the within-stage TC correlation.
857
858 **Identification of stable place cell across stages:**

859 Stable place cells were defined as neurons that (i) exhibited a place field at all imaging
860 stages and (ii) showed tuning-curve (TC) correlations between adjacent stages exceeding
861 a predefined threshold (0.51). The stability threshold (0.51) corresponded to the 95th
862 percentile of TC correlations obtained from 1,000 randomly paired place cells at stage
863 1(Supplementary Fig. 3c).
864
865 **Splitter cell identification:**
866 To identify hippocampal splitter cells, the stem arm of the figure-8 maze was divided into
867 1-cm spatial bins. Place cells with place fields spanning at least five consecutive bins
868 along the stem were included for analysis. For each cell, neural activity was computed at
869 each stem bin across trials, and spatial tuning curves were constructed separately for
870 correct left-turn and right-turn trials. The difference between the two tuning curves was
871 then calculated at each bin. Significance was assessed using a permutation procedure in
872 which left- and right-turn trial labels were randomly shuffled 1,000 times. A cell was
873 classified as a splitter cell if (i) it possessed a place field covering at least five stem-arm
874 bins and (ii) its real tuning-curve difference exceeded the 95th percentile of the shuffled
875 distribution in at least one spatial bin.
876
877 To ensure that splitting activity did not arise from stereotyped speed differences along the
878 stem, we evaluated whether each spatial bin exhibited speed-independent splitting. For
879 each neuron, we first constructed spatially binned activity for every trial. We then
880 performed a linear mixed-effects analysis (MATLAB fitlme) for each stem place cell
881 (defined as cells with a place field > 5 cm along the stem). The model included trial type

882 (left/right) as a categorical predictor and animal speed as a continuous predictor, with
883 spatially binned activity as the dependent variable. A spatial bin was considered to exhibit
884 valid splitting activity if trial type remained a significant predictor of neuronal activity after
885 controlling for speed. Neurons with at least one spatial bin meeting this criterion were
886 classified as splitter cells.
887
888 **Splitter cell quality metrics:**
889 The quality of neuronal splitting activity was assessed using five metrics, computed for
890 identified splitter cells:
891 1) Split extent [79]
892 The proportion of spatial bins along the stem arm that exhibited significant splitting activity.
893 2) Split discriminability.
894 Split discriminability was calculated as the sum of the absolute differences between left-
895 and right-turn tuning curves across all stem bins, normalised by the total summed activity
896 of both tuning curves across those bins.
897 3) Split reliability (Trial-to-trial correlation)
898 This metric quantified the consistency of splitting activity across trials. For each cell,
899 Pearson correlation coefficients were computed between the spatial activity profiles of
900 adjacent trials in the neuron's preferred trajectory direction (e.g., between consecutive
901 left–right trials if the cell preferred the L-R trajectories). Correlations were calculated only
902 within the same imaging session.
903 4) Active split-trial ratio.

904 The proportion of trials in which a splitter cell was active during its high-rate trajectory
905 direction.
906 5) First split trial
907 The trial number at which a cell first is active on its splitting spatial bin.
908
909 **Discriminant classification:**
910 A linear discriminant classifier was trained using 70% of randomly selected correct trials
911 from each imaging session. The classifier was implemented using MATLAB's built-in
912 function fitcdiscr. For each neuron, calcium activity at each time point while the mouse
913 occupied the stem arm served as input features, and the mouse's upcoming turn direction
914 was used as the response variable. Only correct trials (left-right and right-left) were
915 included in both the training and testing sets. The trained classifier was then used to
916 predict turn direction on the remaining 30% of correct trials. This procedure was repeated
917 1,000 times, each with different randomly selected training and testing subsets. Decoding
918 accuracy was computed within 1 cm spatial bins along the stem arm, and session level
919 decoding accuracy was defined as the mean accuracy averaged across all spatial bins.
920
921 **Quantification of Retrospective-Prospective Bias:**
922 We quantified the influence of past versus future behavioural choices on neuronal activity
923 by computing a dissimilarity-based Retrospective-Prospective (RP) bias index, adapted
924 from previously established approaches Varga et al.[39]. Analysis was restricted to
925 recording sessions containing at least three error left trials and three error right trials. For
926 each spatial bin along the stem, we extracted calcium activitity rates from four trial types:

927 RL: correct left; LR: correct right; LL: error left; RR: error right. For each spatial bin,
928 dissimilarity between two trial types was computed as: $D = -\log10(p)$, where p is the
929 Wilcoxon rank-sum test p-value comparing firing-rate distributions across trials. Higher
930 dissimilarity values indicate greater difference in neural activity patterns between the two
931 compared trial types. Four pairwise comparisons were performed: Retrospective
932 comparisons (LL vs. LR; RR vs. RL), Prospective comparisons (LL vs. RL; RR vs. LR).
933 For each spatial bin, we derived: D_{retro}=min[D(LL,LR),D(RR,RL)]; D_{pro}
934 =min[D(LL,RL),D(RR,LR)]. The Retro–Pro (RP) bias index was then computed as: (D_{retro}
935 - D_{pro})/ (D_{retro} + D_{pro}). This value ranges from −1 (purely prospective encoding) to +1
936 (purely retrospective encoding), with values near zero indicating balanced encoding.
937
938 **Statistical tests**
939
940 All statistical analyses and visualisation were performed in MATLAB. Data are presented
941 either as mean ± s.e.m. or as box plots. The significance threshold was set at $p \leq 0.05$.
942 Behavioural performance across training days or trial blocks was analysed using linear
943 mixed-effects models (LMMs). Genotype, Day (or Block) and their interaction (Genotype
944 × Day/Block) were treated as fixed effects, and Mouse ID was included as a random
945 intercept to account for repeated measures. For datasets with multiple imaging sessions
946 per mouse (where each session corresponded to a distinct imaging field of view, with no
947 repeated cells across sessions), linear mixed-effects models included nested random
948 intercepts for MouseID and SessionID to account for within-animal and within-session
949 variability (data ~ 1 + Genotype + (1 | MouseID:SessionID)) . For datasets in which each

mouse contributed only a single imaging session (e.g., DREADD experiments), only MouseID was included as a random effect, as SessionID and MouseID were equivalent in this context. Stable place cells across learning stages were pooled across mice and analysed using non-parametric comparisons. For non-parametric comparisons, effect sizes were reported as rank-biserial correlation (rrb). For linear mixed-effects models, estimates are reported with 95% confidence intervals. For all other comparisons, non-parametric Wilcoxon rank-sum or Wilcoxon signed-rank tests were used to avoid assumptions of normality, unless otherwise specified in the relevant methods. Data points are shown whenever possible, and Bonferroni corrections were applied for multiple comparisons. For datasets displayed as box plots, boxes indicate the interquartile range (IQR; 25th–75th percentiles), the central line denotes the median, and whiskers extend to 1.5 × IQR; points beyond this range are plotted as outliers.

Acknowledgments

We thank Yu Liu and Nawal Zabouri for their help with animal genotyping and daily support, Jina Song for assisting with the behavioural training protocol, and Seigfred Prado for his help with image processing using high-performance computing.

Funding:

Mrs Anne Uren and the Michael Uren Foundation to SRS

EPSRC EP/W024020/1 and EP/W035057/1 to SRS

BBSRC BB/Y514202/1 to SRS

CZI CP-2-1-Schultz to SRS

Author contributions:

Y.L. and S.R.S. conceived and designed the study. Y.L.mainly conducted experiments and collected data under guidance and supervision of S.R.S. and M.A.G., Y.L. and H.Z. analyzed data. M.A.G. and H.Z. contributed to imaging data processing. Y.L. and S.R.S. wrote the paper. All authors discussed and commented on the manuscript.

Competing interests: Authors declare that they have no competing interest.

Data and materials availability: Code and data used to generate the figures described in this paper will be made available via DataDryad at the time of publication, with a DOI to be included here.

Reference

1. Tahami Monfared AA, Byrnes MJ, White LA, Zhang Q. Alzheimer's Disease: Epidemiology and Clinical Progression. *Neurol Ther* **11**, 553-569 (2022).

2. Busche MA, Hyman BT. Synergy between amyloid-β and tau in Alzheimer's disease. *Nature Neuroscience* **23**, 1183-1193 (2020).

3. Xiong H*, et al.* Cholesterol retention in Alzheimer's brain is responsible for high β-and γ-secretase activities and Aβ production. *Neurobiology of disease* **29**, 422-437 (2008).

4. Condello C, Yuan P, Schain A, Grutzendler J. Microglia constitute a barrier that prevents neurotoxic protofibrillar Aβ42 hotspots around plaques. *Nat Commun* **6**, 6176 (2015).

5. Bellaver B*, et al.* Astrocyte reactivity influences amyloid-β effects on tau pathology in preclinical Alzheimer's disease. *Nature medicine* **29**, 1775-1781 (2023).

6. Frere S, Slutsky I. Alzheimer's Disease: From Firing Instability to Homeostasis Network Collapse. *Neuron* **97**, 32-58 (2018).

7. Hort J, Laczó J, Vyhnálek M, Bojar M, Bureš J, Vlček K. Spatial navigation deficit in amnestic mild cognitive impairment. *Proceedings of the National Academy of Sciences* **104**, 4042-4047 (2007).

8. Newton C*, et al.* Entorhinal-based path integration selectively predicts midlife risk of Alzheimer's disease. *Alzheimers Dement* **20**, 2779-2793 (2024).

9. Hope T, Tilling KM, Gedling K, Keene JM, Cooper SD, Fairburn CG. The structure of wandering in dementia. *International Journal of Geriatric Psychiatry* **9**, 149-155 (1994).

10. Vyas Y, Montgomery JM, Cheyne JE. Hippocampal deficits in amyloid-β-related rodent models of Alzheimer's disease. *Frontiers in neuroscience* **14**, 266 (2020).

11. West MJ, Coleman PD, Flood DG, Troncoso JC. Differences in the pattern of hippocampal neuronal loss in normal ageing and Alzheimer's disease. *The lancet* **344**, 769-772 (1994).

12. Mufson EJ*, et al.* Hippocampal plasticity during the progression of Alzheimer's disease. *Neuroscience* **309**, 51-67 (2015).

13. Cacucci F, Yi M, Wills TJ, Chapman P, O'Keefe J. Place cell firing correlates with memory deficits and amyloid plaque burden in Tg2576 Alzheimer mouse model. *Proceedings of the National Academy of Sciences* **105**, 7863-7868 (2008).

14. Zhao R, Fowler SW, Chiang AC, Ji D, Jankowsky JL. Impairments in experience-dependent scaling and stability of hippocampal place fields limit spatial learning in a mouse model of Alzheimer's disease. *Hippocampus* **24**, 963-978 (2014).

15. Lin X*, et al.* Spatial coding defects of hippocampal neural ensemble calcium activities in the triple-transgenic Alzheimer's disease mouse model. *Neurobiol Dis* **162**, 105562 (2022).

16. Mably AJ, Gereke BJ, Jones DT, Colgin LL. Impairments in spatial representations and rhythmic coordination of place cells in the 3xTg mouse model of Alzheimer's disease. *Hippocampus* **27**, 378-392 (2017).

17. Prince SM, Paulson AL, Jeong N, Zhang L, Amigues S, Singer AC. Alzheimer's pathology causes impaired inhibitory connections and reactivation of spatial codes during spatial navigation. *Cell reports* **35**, (2021).

18. Zhang H*, et al.* Degenerate mapping of environmental location presages deficits in object-location encoding and memory in the 5xFAD mouse model for Alzheimer's disease. *Neurobiol Dis* **176**, 105939 (2023).

19. Wood ER, Dudchenko PA, Robitsek RJ, Eichenbaum H. Hippocampal neurons encode information about different types of memory episodes occurring in the same location. *Neuron* **27**, 623-633 (2000).

20. Frank LM, Brown EN, Wilson M. Trajectory encoding in the hippocampus and entorhinal cortex. *Neuron* **27**, 169-178 (2000).

21. Duvelle E, Grieves RM, van der Meer MAA. Temporal context and latent state inference in the hippocampal splitter signal. *Elife* **12**, (2023).

22. Chapman PF*, et al.* Impaired synaptic plasticity and learning in aged amyloid precursor protein transgenic mice. *Nat Neurosci* **2**, 271-276 (1999).

23. Zhao X, Hsu CL, Spruston N. Rapid synaptic plasticity contributes to a learned conjunctive code of position and choice-related information in the hippocampus. *Neuron* **110**, 96-108 e104 (2022).

24. Kim SM, Frank LM. Hippocampal lesions impair rapid learning of a continuous spatial alternation task. *PLoS One* **4**, e5494 (2009).

25. Gerlai R. A new continuous alternation task in T-maze detects hippocampal dysfunction in mice. A strain comparison and lesion study. *Behav Brain Res* **95**, 91-101 (1998).

26. Forner S*, et al.* Systematic phenotyping and characterization of the 5xFAD mouse model of Alzheimer's disease. *Sci Data* **8**, 270 (2021).

27. Girard SD*, et al.* Onset of hippocampus‐dependent memory impairments in 5XFAD transgenic mouse model of Alzheimer's disease. *Hippocampus* **24**, 762-772 (2014).

28. Gu Z, Yakel JL. Timing-dependent septal cholinergic induction of dynamic hippocampal synaptic plasticity. *Neuron* **71**, 155-165 (2011).

29. Oakley H*, et al.* Intraneuronal β-amyloid aggregates, neurodegeneration, and neuron loss in transgenic mice with five familial Alzheimer's disease mutations: potential factors in amyloid plaque formation. *Journal of Neuroscience* **26**, 10129-10140 (2006).

30. Pádua MS, Guil-Guerrero JL, Lopes PA. Behaviour Hallmarks in Alzheimer’s Disease 5xFAD Mouse Model. *International Journal of Molecular Sciences* **25**, 6766 (2024).

31. Morris JC*, et al.* Mild cognitive impairment represents early-stage Alzheimer disease. *Arch Neurol* **58**, 397-405 (2001).

32. Caselli RJ, Reiman EM. Characterizing the preclinical stages of Alzheimer's disease and the prospect of presymptomatic intervention. *J Alzheimers Dis* **33 Suppl 1**, S405-416 (2013).

33. Kimura R, Ohno M. Impairments in remote memory stabilization precede hippocampal synaptic and cognitive failures in 5XFAD Alzheimer mouse model. *Neurobiology of disease* **33**, 229-235 (2009).

34. Devi L, Ohno M. Cognitive benefits of memantine in Alzheimer's 5XFAD model mice decline during advanced disease stages. *Pharmacol Biochem Behav* **144**, 60-66 (2016).

35. Lever C, Wills T, Cacucci F, Burgess N, O'Keefe J. Long-term plasticity in hippocampal place-cell representation of environmental geometry. *Nature* **416**, 90-94 (2002).

36. Ziv Y*, et al.* Long-term dynamics of CA1 hippocampal place codes. *Nat Neurosci* **16**, 264-266 (2013).

37. Ainge JA, van der Meer MA, Langston RF, Wood ER. Exploring the role of context-dependent hippocampal activity in spatial alternation behavior. *Hippocampus* **17**, 988-1002 (2007).

38. Ito HT, Zhang SJ, Witter MP, Moser EI, Moser MB. A prefrontal-thalamo-hippocampal circuit for goal-directed spatial navigation. *Nature* **522**, 50-55 (2015).

39. Varga V, Petersen P, Zutshi I, Huszar R, Zhang Y, Buzsaki G. Working memory features are embedded in hippocampal place fields. *Cell Rep* **43**, 113807 (2024).

40. Catanese J, Viggiano A, Cerasti E, Zugaro MB, Wiener SI. Retrospectively and Prospectively Modulated Hippocampal Place Responses Are Differentially Distributed along a Common Path in a Continuous T-Maze. *The Journal of Neuroscience* **34**, 13163-13169 (2014).

41. Etter G, van der Veldt S, Choi J, Williams S. Optogenetic frequency scrambling of hippocampal theta oscillations dissociates working memory retrieval from hippocampal spatiotemporal codes. *Nat Commun* **14**, 410 (2023).

42. Youmans KL*, et al.* Intraneuronal Aβ detection in 5xFAD mice by a new Aβ-specific antibody. *Molecular neurodegeneration* **7**, 1-14 (2012).

43. Crouzin N*, et al.* Area-specific alterations of synaptic plasticity in the 5XFAD mouse model of Alzheimer's disease: dissociation between somatosensory cortex and hippocampus. *PLoS One* **8**, e74667 (2013).

44. Martorell AJ*, et al.* Multi-sensory gamma stimulation ameliorates Alzheimer’s-associated pathology and improves cognition. *Cell* **177**, 256-271. e222 (2019).

45. Zhang H*, et al.* Degenerate mapping of environmental location presages deficits in object-location encoding and memory in the 5xFAD mouse model for Alzheimer's disease. *Neurobiology of disease* **176**, 105939 (2023).

46. Lei Y*, et al.* Chronic social isolation-unpredictable stress induces early-onset cognitive deficits and exacerbates Abeta accumulation in the 5xFAD mouse model of Alzheimer's disease. *Mol Psychiatry* **30**, 4720-4735 (2025).

47. Miranda AM*, et al.* Excess synaptojanin 1 contributes to place cell dysfunction and memory deficits in the aging hippocampus in three types of Alzheimer’s disease. *Cell reports* **23**, 2967-2975 (2018).

48. Busche MA*, et al.* Critical role of soluble amyloid-beta for early hippocampal hyperactivity in a mouse model of Alzheimer's disease. *Proc Natl Acad Sci U S A* **109**, 8740-8745 (2012).

49. Jun H, Bramian A, Soma S, Saito T, Saido TC, Igarashi KM. Disrupted place cell remapping and impaired grid cells in a knockin model of Alzheimer's disease. *Neuron* **107**, 1095-1112. e1096 (2020).

50. Zemla R, Moore JJ, Hopkins MD, Basu J. Task-selective place cells show behaviorally driven dynamics during learning and stability during memory recall. *Cell reports* **41**, (2022).

51. Kentros CG, Agnihotri NT, Streater S, Hawkins RD, Kandel ER. Increased attention to spatial context increases both place field stability and spatial memory. *Neuron* **42**, 283-295 (2004).

52. Climer JR, Davoudi H, Oh JY, Dombeck DA. Hippocampal representations drift in stable multisensory environments. *Nature* **645**, 457-465 (2025).

53. Vaidya SP, Li G, Chitwood RA, Li Y, Magee JC. Formation of an expanding memory representation in the hippocampus. *Nat Neurosci* **28**, 1510-1518 (2025).

54. Sun C, Yang WN, Martin J, Tonegawa S. Hippocampal neurons represent events as transferable units of experience. *Nature Neuroscience* **23**, 651-U117 (2020).

55. Eichenbaum H. Time cells in the hippocampus: a new dimension for mapping memories. *Nat Rev Neurosci* **15**, 732-744 (2014).

56. Gauthier JL, Tank DW. A Dedicated Population for Reward Coding in the Hippocampus. *Neuron* **99**, 179-193 e177 (2018).

57. Kim EJ, Park S, Schuessler BP, Boo H, Cho J, Kim JJ. Disruption of hippocampal-prefrontal neural dynamics and risky decision-making in a mouse model of Alzheimer's disease. *Cell Rep* **44**, 116081 (2025).

58. Andersen JV*, et al.* Hippocampal disruptions of synaptic and astrocyte metabolism are primary events of early amyloid pathology in the 5xFAD mouse model of Alzheimer's disease. *Cell Death & Disease* **12**, (2021).

59. Grienberger C, Magee JC. Entorhinal cortex directs learning-related changes in CA1 representations. *Nature* **611**, 554-+ (2022).

60. Bartus RT, Dean RL, 3rd, Beer B, Lippa AS. The cholinergic hypothesis of geriatric memory dysfunction. *Science* **217**, 408-414 (1982).

61. Chen ZR, Huang JB, Yang SL, Hong FF. Role of Cholinergic Signaling in Alzheimer's Disease. *Molecules* **27**, (2022).

62. Ballinger EC, Ananth M, Talmage DA, Role LW. Basal Forebrain Cholinergic Circuits and Signaling in Cognition and Cognitive Decline. *Neuron* **91**, 1199-1218 (2016).

63. Vandecasteele M*, et al.* Optogenetic activation of septal cholinergic neurons suppresses sharp wave ripples and enhances theta oscillations in the hippocampus. *Proc Natl Acad Sci U S A* **111**, 13535-13540 (2014).

64. Yan H*, et al.* The Lesion Analysis of Cholinergic Neurons in 5XFAD Mouse Model in the Three-Dimensional Level of Whole Brain. *Molecular Neurobiology* **55**, 4115-4125 (2018).

65. Ravassard P*, et al.* Multisensory control of hippocampal spatiotemporal selectivity. *Science* **340**, 1342-1346 (2013).

66. Aghajan ZM, Acharya L, Moore JJ, Cushman JD, Vuong C, Mehta MR. Impaired spatial selectivity and intact phase precession in two-dimensional virtual reality. *Nat Neurosci* **18**, 121-128 (2015).

67. Go MA*, et al.* Place cells in head-fixed mice navigating a floating real-world environment. *Frontiers in cellular neuroscience* **15**, 618658 (2021).

68. Arnold M*, et al.* Sex and APOE ε4 genotype modify the Alzheimer's disease serum metabolome. *Nat Commun* **11**, 1148 (2020).

69. Sohn D*, et al.* Sex differences in cognitive decline in subjects with high likelihood of mild cognitive impairment due to Alzheimer's disease. *Scientific reports* **8**, 7490 (2018).

70. Poon CH*, et al.* Sex differences between neuronal loss and the early onset of amyloid deposits and behavioral consequences in 5xFAD transgenic mouse as a model for Alzheimer's disease. *Cells* **12**, 780 (2023).

71. Sadleir KR, Eimer WA, Cole SL, Vassar R. Aβ reduction in BACE1 heterozygous null 5XFAD mice is associated with transgenic APP level. *Molecular neurodegeneration* **10**, 1-16 (2015).

72. O'Leary TP, Brown RE. Visuo-spatial learning and memory impairments in the 5xFAD mouse model of Alzheimer's disease: Effects of age, sex, albinism, and motor impairments. *Genes, Brain and Behavior* **21**, e12794 (2022).

73. Oblak AL*, et al.* Comprehensive Evaluation of the 5XFAD Mouse Model for Preclinical Testing Applications: A MODEL-AD Study. *Front Aging Neurosci* **13**, 713726 (2021).

74. Popugaeva E, Pchitskaya E, Bezprozvanny I. Dysregulation of intracellular calcium signaling in Alzheimer's disease. *Antioxidants & redox signaling* **29**, 1176-1188 (2018).

75. Dombeck DA, Harvey CD, Tian L, Looger LL, Tank DW. Functional imaging of hippocampal place cells at cellular resolution during virtual navigation. *Nat Neurosci* **13**, 1433-1440 (2010).

76. Zhou H*, et al.* Cholinergic modulation of hippocampal calcium activity across the sleep-wake cycle. *Elife* **8**, (2019).

77. Giovannucci A*, et al.* CaImAn an open source tool for scalable calcium imaging data analysis. *Elife* **8**, e38173 (2019).

78. Skaggs W, Mcnaughton B, Gothard K. An information-theoretic approach to deciphering the hippocampal code. *Advances in neural information processing systems* **5**, (1992).

79. Kinsky NR, Mau W, Sullivan DW, Levy SJ, Ruesch EA, Hasselmo ME. Trajectory-modulated hippocampal neurons persist throughout memory-guided navigation. *Nat Commun* **11**, 2443 (2020).

Supplementary Information

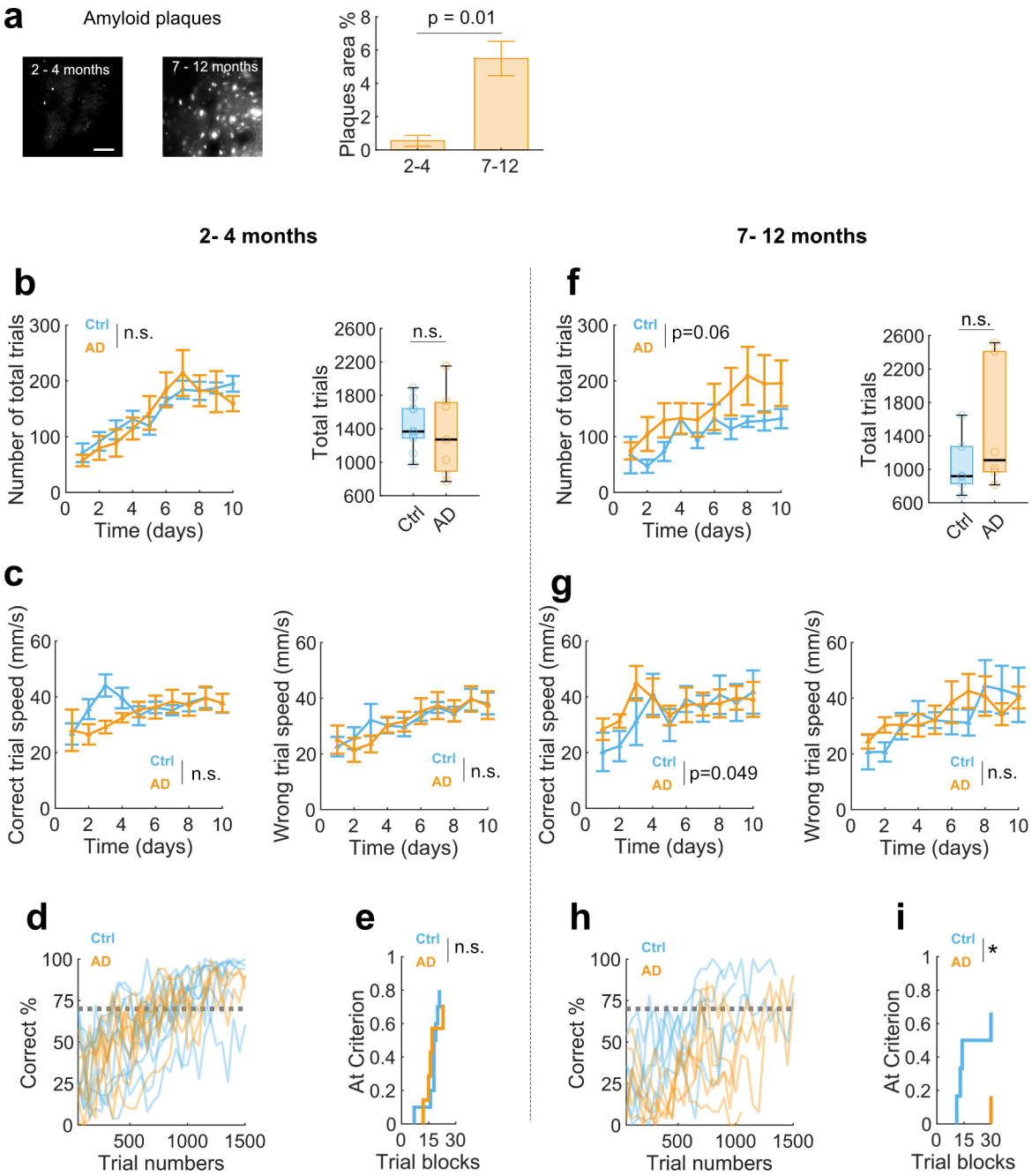

Supplementary Figure 1. Head-fixed behavioural training in 5xFAD mice (related to Figure 1)

a. Representative *in vivo* imaging of amyloid plaques in hippocampal CA1 regions, labelled with Methoxy-X04. Quantification shows the percentage area of amyloid plaques relative to the total field of view (FOV) in 5xFAD mice aged 2–4 months (n = 3 mice) and 7–12 months (n = 3 mice). Data are presented as mean ± s.e.m.; comparisons were performed using a two-sided Student's t-test. Scale bar, 100 μm.

b. *Left:* Mean total number of trials completed per training day (mean ± s.e.m.) for 2–4-month-old mice, analysed using a linear mixed-effects model (LMM). *Right:* Cumulative number of trials completed by each mouse across all training sessions. Statistical comparisons were performed using a two-sided Wilcoxon rank-sum test.
c. *Left:* average running speeds across all correct trials across training sessions. *Right:* average running speeds across all error trials across training sessions. Group differences were evaluated using LMM.
d. Alternation performance across training days segmented into 50-trial blocks (up to 30 blocks) for 2–4-month-old mice. Individual mouse performance is shown as lines.
e. Proportion of mice reaching the acquisition criterion (>70% correct across four consecutive trial blocks) and the corresponding trial block at which criterion was achieved. Statistical significance was assessed using a log-rank test.
f-i. Same analyses as in panels **b-e** but for mice aged 7–12 months.

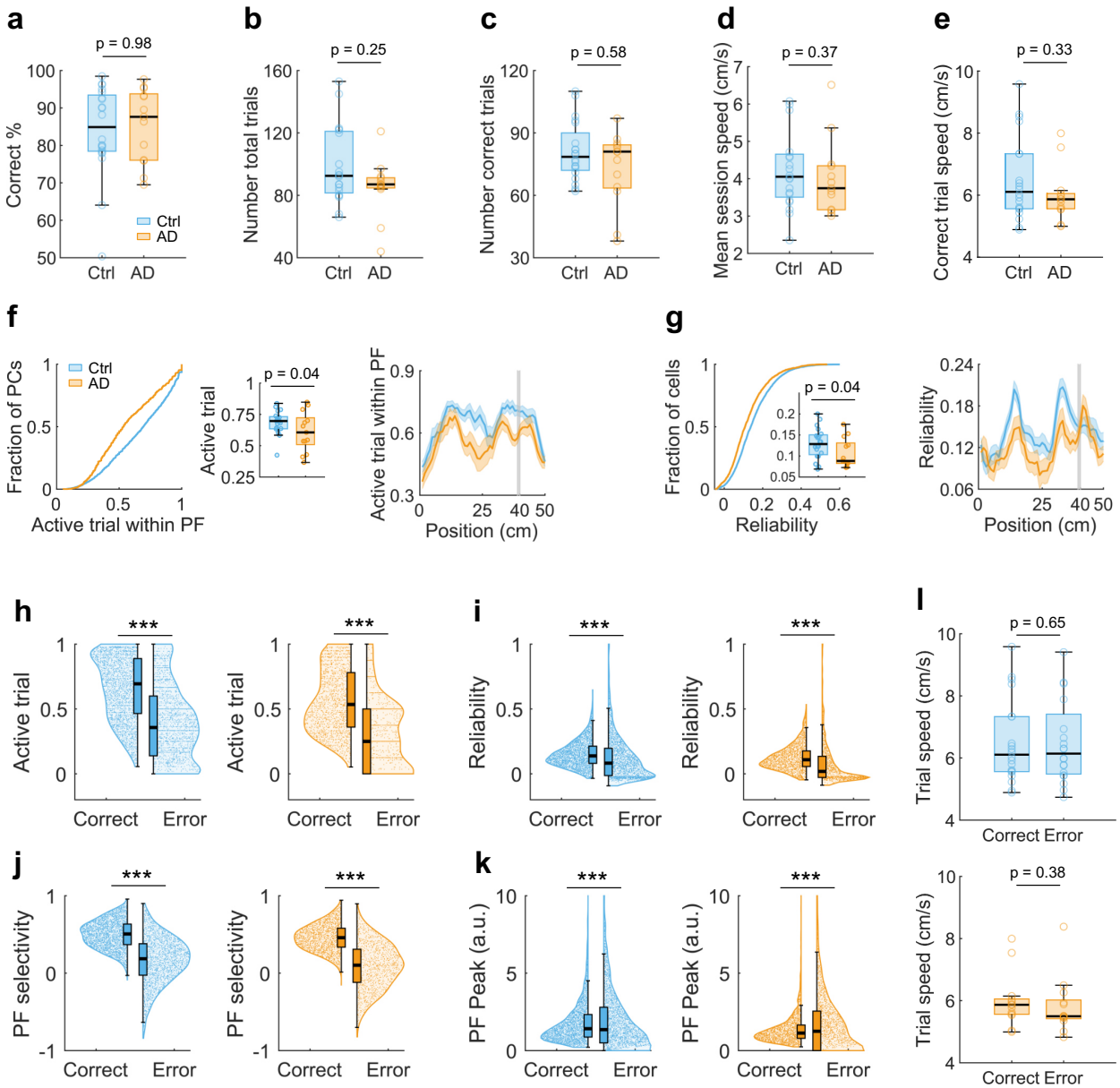

Supplementary Figure 2 | Behavioural performance during imaging and CA1 place cell properties in correct versus error trials (related to Fig. 2)

a-e. Behavioural measures per imaging session: (a) alternation accuracy, (b) total trials, (c) correct trials, (d) mean speed including speeds below 8 mm/s, and (e) mean speed during correct trials above 8 mm/s. Two-sided Wilcoxon rank-sum tests.
f. Left: cumulative distribution of active-trial ratio, defined as the proportion of trials in which a cell was active within its place field. Inset shows session medians. Right: active-trial ratio across linearised maze position.
g. Same as f, showing adjacent trial-to-trial tuning curve correlation (pairwise Pearson's r), calculated only from trials where the cell was active. LMM used for Ctrl vs AD comparison.
h-k. Place cell properties in correct and error trials: (h) active-trial ratio, (i) trial-to-trial reliability, (j) in-field versus out-of-field selectivity, and (k) peak in-field activity. Two-sided Wilcoxon signed-rank tests.

I. Mean trial speed per session during correct and error trials.
Control group includes 2952 cells from 20 sessions (10 mice), 5xFAD group includes 1791 cells from 13 sessions (7 mice).

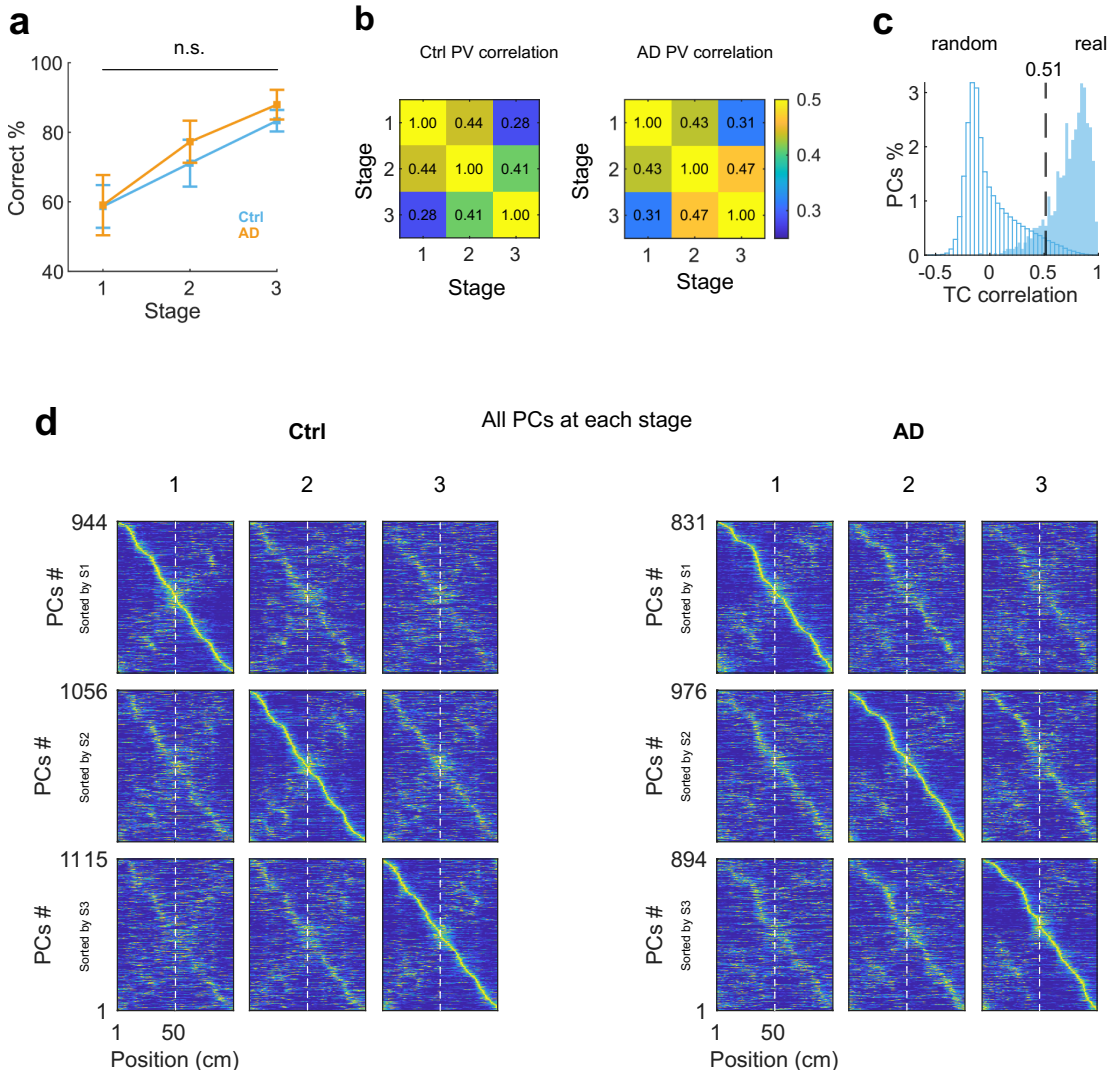

Supplementary Figure 3. Place cells across training stages (related to Figure 3)

a. Behavioural alternation performance across imaging stages. The grey dotted line marks the 70% performance criterion. LMM test.
b. PV correlation of all cells between stages.
c. Tuning curve (TC) correlation threshold used to define stable place cells across days. Stage-1 TC correlations were computed by correlating tuning curves generated from odd and even trials within the same stage. The stability threshold was set at the 95th percentile of 1,000 randomly paired cell correlations.
d. Place fields along the linearised trajectory, sorted by place cell identity at each imaging stage. The left side of the white dotted line represents left-to-right trials; the right side represents right-to-left trials.
Data represent as mean ± s.e.m, Control; 10 imaging sessions from 5 mice per stage. 5xFAD: 7 imaging sessions from 4 mice per stage.

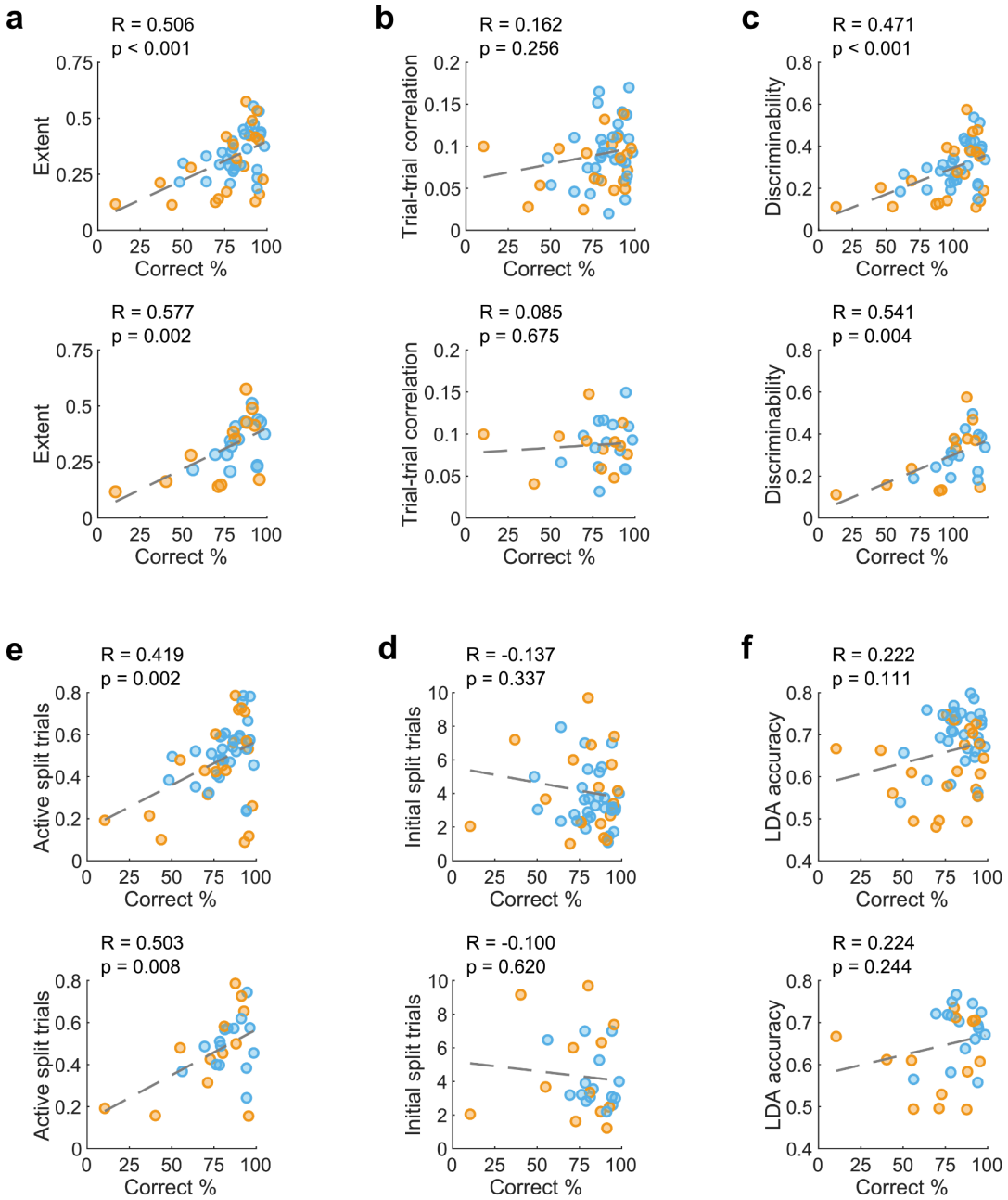

Supplementary Figure 4. Correlation between hippocampal splitter cell quality and behavioural performance (related to Figure 4)

Pearson correlations between splitter-cell quality metrics and behavioural performance.

a. Splitting extent (top: per FOV; bottom: per mouse).

b. Trial-to-trial spatial correlation.

c. Discriminability between high- and low-rate trajectories.

d. Proportion of trials in which splitting activity was expressed.

e. Trial number at which splitting activity first emerged.

f. Decoding accuracy of a discriminant analysis classifier. Correlation coefficients and p values are shown in each panel. Data were pooled from 2–4 month-old and 7–12 month-old control (N=16) and 5xFAD mice (N = 13).

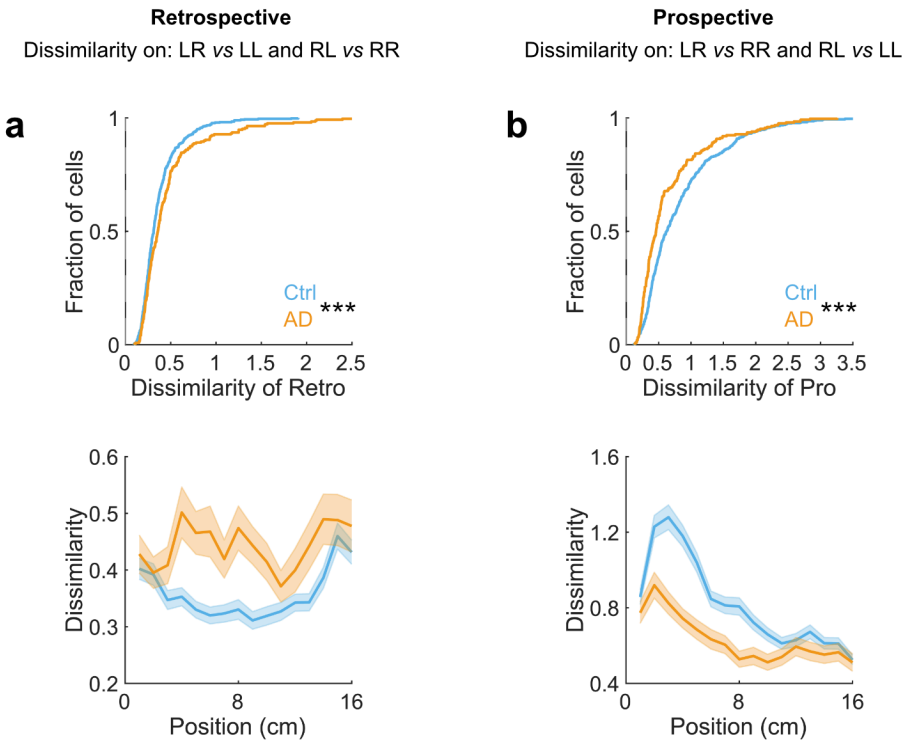

Supplementary Figure 5. Encoding on retrospective and prospective trajectories (related to Figure 5)

a. Top: Dissimilarity values for retrospective trajectories (e.g., LR vs. LL trials; RL vs. RR trials). Dissimilarity was computed as the $-\log_{10}$(p value) from Wilcoxon ranksum test comparing cell activity rates at each spatial bin across the two trial types. Bottom: Retrospective dissimilarity plotted across stem positions. Genotype effect: $F(15, 10809) = 3.07$, $p < 0.001$; Genotype × bin interaction: $F(15, 10809) = 1.52$, $p = 0.089$; two-way ANOVA. Lower dissimilarity values indicate stronger retrospective trajectory encoding.
b. Same analysis as in panel **a**, but for prospective trajectories (e.g., LR vs. RR trials; RL vs. LL trials). Genotype effect: $F(15, 10904) = 21.2$, $p < 0.001$; Genotype × bin interaction: $F(15, 10904) = 3.47$, $p < 0.001$; two-way ANOVA.

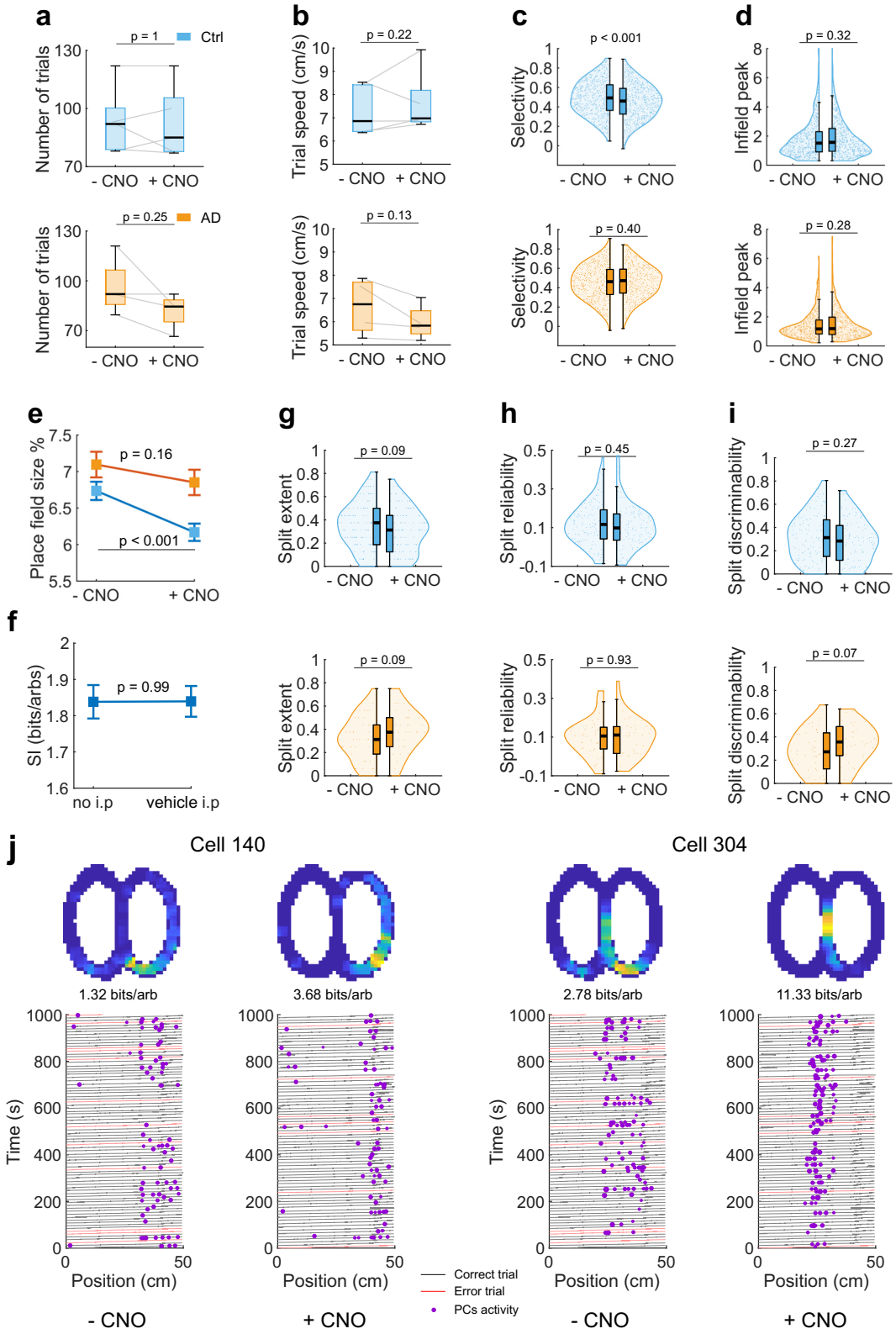

Supplementary Figure 6. Behaviour and hippocampal CA1 encoding after basal forebrain cholinergic activation via DREADDs

a. Number of trials completed after vehicle and CNO injection.
b. Average Trial speed after vehicle and CNO injection.
c-d. CA1 place cell metrics following vehicle and CNO injection (left to right): in-field versus out-of-field selectivity and peak in-field activity.
e. Place field size of CA1 place cells after vehicle and CNO injection.
f. Place cells information during correct trials after no i.p injection and vehicle i.p injection in DREADD (hM3Dq) injectied mice.
g-i. Stem place cell metrics following vehicle and CNO injection (left to right): split extent, trial-to-trial correlation in the high-rate trajectory direction, and the difference between high- and low-rate trajectory activity.
j. Representative examples of CA1 place cell activity after vehicle and CNO administration in a AD mouse. Magenta dots indicate cell calcium activity; grey lines indicate correct trials, and red lines indicate error trials. Cell ID 140 exhibited a place field on the reward arm, and Cell ID 304 showed a stem arm place field with splitting activity.
Data were analysed using linear mixed-effects models with DREADD activation (CNO vs vehicle) as a fixed effect and Mouse ID as a random intercept. Ctrl: 964 detected neurons; place cells: 697 (140 stem-place cells) after vehicle, and 522 (122 stem place cells) after CNO; 5 mice. AD: 777 detected neurons; place cells: 522 (46 stem place cells) after vehicle, and 449 (41 stem place cells) after CNO; 4 mice.